Pergamon

Int. J. Solids Structures Vol. 35, No. 24, pp. 3177–3211, 1998

0020–7683/98 $19.00 + .00

PII: S0020–7683(98)00010–9

TIME EVOLUTION OF STRESS REDISTRIBUTION AROUND MULTIPLE FIBER BREAKS IN A COMPOSITE WITH VISCOUS AND VISCOELASTIC MATRICES

IRENE J. BEYERLEIN,* S. LEIGH PHOENIX
Department of Theoretical and Applied Mechanics, Cornell University, Ithaca, NY 14853, U.S.A.

and

RISHI RAJ
Department of Mechanical Engineering, University of Colorado, Boulder, CO 80309-0427, U.S.A.

(*Received* 16 *June* 1997; *and in revised form* 17 *December* 1997)

Abstract—We develop an efficient computational technique, called viscous break interaction (VBI), to determine the time evolution of fiber and matrix stresses around a large, arbitrary array of fiber breaks in a unidirectional composite with a matrix that creeps. The matrix is assumed to be linearly viscoelastic or viscous in shear following a power-law in time (creep exponent $0 \leqslant \alpha \leqslant 1$), and interface debonding or slip is not permitted. Such a law is applicable to polymeric matrices over a wide range of temperatures or to a viscous, glassy interphase in a ceramic composite with elongated microstructure. Specifically, we consider an infinitely large, 2-D composite lamina in the shear-lag framework of Hedgepeth, and the multiple break formulation is built on weighted superposition using influence functions based on the response to an isolated break. We apply the method to problems involving large transverse cracks (i.e., aligned, contiguous breaks), fully bridged cracks, and arrays of interacting, longitudinally staggered breaks. In each case we calculate the time evolution of stress concentrations and displacements of individual fibers. In comparing cracks vs spatially staggered breaks, the results reveal interesting contrasts in the time variation of both peak fiber stress concentrations and break opening displacements. In the latter case, we see behavior consistent with the three stages of creep, and show how the local fiber tensile stresses can rise (and subsequently even fall) at rates depending on various microstructural length scales. The motivation for developing VBI is to provide the computational framework for modeling the statistical features of the lifetime of composites in creep-rupture resulting from an accumulation of many fiber breaks and ultimately localization and collapse.

NOMENCLATURE

α	power law exponent in $J(\mathscr{T})$, $0 \leqslant \alpha \leqslant 1$
A	fiber cross sectional area
β	constant solely dependent on α
C_θ	$\sin(\theta/2)$
δ	1/2 the length of each fiber and matrix element
$\delta(\mathscr{T})$	delta function
erfc(·)	complementary error function
E	fiber Young's modulus
$G(\mathscr{T})$	matrix relaxation function
G_e	matrix elastic shear modulus
$\underline{\mathscr{G}}(s)$	Laplace transform of the relaxation modulus
γ	Euler's constant, $\gamma \cong 0.5772$
$\gamma_n(x, \mathscr{T})$	shear strain in matrix bay n at time $\mathscr{T}$
$\Gamma(\cdot)$	gamma function
$\Gamma_n(\xi, t)$	normalized shear strain in matrix region n
$\Gamma_n^u(\xi, t)$	normalized matrix shear strain due to isolated fiber break
$\Gamma_n^{u,e}(\xi)$	normalized matrix shear strain due to isolated fiber break for linear elastic matrix
$\partial\Gamma_n(\xi, t)/\partial t$	normalized matrix bay shear strain rate
h	fiber diameter and lamina thickness

*Present address: Center for Materials Science, Mail Stop G755, Los Alamos National Laboratory, Los Alamos, NM 87545, U.S.A.

η	constant matrix viscosity, $\eta = t_c/J_e$
$I(t)$	indicator function
$J(\mathscr{T})$	matrix creep compliance function
$J_0(\mathscr{T})$	time-dependent component of the matrix creep compliance function
$J_1(\mathscr{T})$	matrix creep compliance function, including both the elastic and time-dependent components
$\mathscr{J}(t)$	creep compliance function normalized
$\underline{\mathscr{J}}_0(s)$	Laplace transform of the normalized $\mathscr{J}_0(t)$
$\underline{\mathscr{J}}_1(s)$	Laplace transform of the normalized $\mathscr{J}_1(t)$
J_e	constant in $J(\mathscr{T})$ with dimensions [stress^{-1}]
$\mathscr{K}_j(t)$	time dependent weighting function for fiber break j
$l_t(\mathscr{T})$	overload length on nearest fiber due to an isolated break
L	normalized axial distance of staggered breaks from mid-plane
$\mathbf{L}$	the Laplace operator
$L_n(\xi, t)$	normalized axial load of fiber n under unit compressive load and zero far field load
$L_n^u(\xi, t)$	normalized axial load due to isolated fiber break under unit compressive load for a creeping matrix
$L_n^{u,e}(\xi)$	normalized axial load due to isolated fiber break under unit compressive load for linear elastic matrix
$\mathscr{L}_n(z)$	$L_n^u(\xi, t)$ for the linearly viscous and viscoelastic cases
$\Lambda_{ij}(t)$	time dependent transmission function between fiber breaks i and j
m	longitudinal fiber or matrix element number
n	transverse fiber or matrix element number
p^*	far field load per fiber
$p_n(x, \mathscr{T})$	axial load of fiber n at time $\mathscr{T}$
P	normalized far field load
$P_n(\xi, t)$	normalized axial load of fiber n under uniform P
$P_n^e(\xi)$	elastic solution as described in Hedgepeth (1961)
r	total number of fiber breaks
s	Laplace transform variable
$\mathrm{sgn}(\xi)$	sign function
t	dimensionless time
$\mathscr{T}$	actual time
$\mathscr{T}_c$	time constant in $J(\mathscr{T})$
$\tau_n(x, \mathscr{T})$	shear stress of matrix region n at time $\mathscr{T}$
$T_n(\xi, t)$	normalized matrix shear stress for region n
$T_n^u(\xi, t)$	normalized matrix shear stress due to isolated fiber break
$T_n^{u,e}(\xi)$	normalized matrix shear stress due to isolated fiber break for linear elastic matrix
$u_n(x, \mathscr{T})$	axial displacement of fiber n at time $\mathscr{T}$
$U_n(\xi, t)$	normalized dimensionless axial displacement of fiber n
$\underline{\mathscr{U}}_n(\xi, s)$	Laplace transform $U_n(\xi, t)$
$V_n(\xi, t)$	normalized displacement of fiber n under unit compressive load and zero far field load
$V_n^u(\xi, t)$	normalized fiber displacements due to isolated fiber break under unit compressive load and zero far field load
$\underline{\mathscr{V}}_n(\xi, s)$	Laplace transform $V_n^u(\xi, t)$
$V_n^{u,e}(\xi)$	normalized axial displacement due to isolated fiber break under unit compressive load for linear elastic matrix
w	width of the matrix region
x	fiber axial coordinate
ξ	dimensionless fiber axial coordinate (time dependent analysis)
z	similarity variable $z = \xi/t^{\alpha/2}$ or $z = \beta\xi/t^{\alpha/2}$

1. INTRODUCTION

1.1. *Overview of the problem*

Advanced fiber-reinforced composites with polymer, metal or ceramic matrices are promising candidates for many high temperature, structural applications, such as pressure vessels, centrifuges, and aircraft and automotive engine components. Such structures are often loaded in service at a substantial fraction of their instantaneous strengths, and depending on the sustained load level and temperature, may eventually fail in stress-rupture (or creep-rupture). In small, uniformly loaded, laboratory specimens, deformation over time may exhibit distinct primary and secondary (steady-state) stages of creep, and stress rupture may occur as a rapid, though measurable, increase in strain rate (tertiary creep), or may occur abruptly at the end of the steady-state stage. In larger, more heterogeneous specimens, instability may occur due to critical damage growth in one or more highly localized regions, which typically are very difficult to detect using global measurements. Typically large variability is associated with such failures leading to great difficulty in reliably forecasting component lifetime.

A major contributor to material breakdown is creep of the matrix in shear around fiber breaks and discontinuities. In polymer matrix composites, matrices exhibit approximately linear viscoelastic behavior at moderate temperatures (Haddad and Iyer, 1996; Kibler and Carter, 1979) and roughly linear viscous behavior near the glass transition temperature (Raghavan and Meshii, 1996). In advanced ceramic composites with elongated microstructure, such as those based on silicon nitride, softening of the glassy, viscous matrix phase at high temperatures is largely responsible for overall creep (Evans and Rana, 1980; Tsai and Raj, 1982). Local matrix creep strains in shear are typically much greater than globally measured creep strains for the material.

Creep damage accumulation is well known to be difficult to model. While idealized analytical results and scalings can provide considerable insight, realistic modeling requires efficient numerical methods coupled with Monte Carlo simulation. Given the statistical nature of stress rupture (Phoenix *et al.*, 1988; Otani *et al.*, 1991; Menon *et al.*, 1994), such simulations can predict global creep strain vs time, allow study of the stochastic evolution of local damage and the onset of instabilities immediately preceding failure, and ultimately help determine overall lifetime distributions in terms of material volume and micromechanical parameters. These models will be useful in reliability-based design, where lifetime predictions may be desired for load levels yielding very low probabilities of failure, say 10^{-d} (where $d \geqslant 4$). Such forecasts would require at least 10^{d+1} Monte Carlo replications.

The progression of creep damage is governed by the time-varying stress redistribution around the current damage state, described in this work in terms of fiber breaks. Therefore, a necessary component in a simulation model is a realistic, point-for-point stress analysis that can handle computationally fiber breaks in any pattern. To accommodate many sequential breaks in a sufficiently large material replicated a large number of times, such a stress analysis must be extremely fast. With this requirement in mind, the present work develops a computational mechanics technique, called viscous break interaction (VBI), to calculate the time-dependent stress redistribution due to an arbitrary array of fiber breaks in a composite lamina with an infinite number of fibers (See Fig. 1).

The foundation of the VBI model is similar to that in Lagoudas *et al.* (1989), in the respect that both build on the classic shear-lag model of Hedgepeth (1961). Accordingly, the role of the matrix is to deform and support stresses primarily in shear, while the fibers are the primary load bearing component, which remain time-independent and linearly elastic. The matrix is taken to be linearly viscous or viscoelastic and is well-bonded to the fiber. Because of its importance in applications, the special case of a Newtonian viscous matrix is examined in some detail.

Lagoudas *et al.* (1989) focused on a single row of a few, transversely aligned, contiguous fiber breaks but gave no indication of how to treat a general arrangement of breaks. In VBI, the problem is reformulated to handle such arrays in a superposition framework using influence functions. Another key difference between VBI and other numerical schemes, such as finite element and spring network models, is that the computation time is tied to the volume of damage (primarily the number of fiber breaks) and not the entire composite volume. To greatly increase the numerical efficiency and speed of calculation, the initial elastic shear component in the matrix is neglected. Despite this simplification, VBI can obtain remarkably good estimates of the initial elastic response, so that in reality very little is lost. Nonetheless, it is the time-dependent component of the matrix shear strain which results in significant fiber stress redistribution over time from breaks and dominates the elastic part.

To date a few "damage-dependent" (rather than volume-dependent) computational mechanics techniques, like VBI, have been developed (Sastry and Phoenix, 1993; Zhou and Curtin, 1995) for large scale simulations of elastic failure in fibrous composites (Ibnabdeljalil and Curtin, 1996; Beyerlein and Phoenix, 1997a, b) and large scale matrix plasticity and interfacial sliding (Beyerlein and Phoenix, 1996, 1997c). All these methods have made use of certain simplifying assumptions, such as the shear-lag model. Nevertheless it has been shown (Beyerlein *et al.*, 1996) that the 2-D Hedgepeth shear-lag model produces stress fields consistent with linear elasticity and linear elastic fracture mechanics for long rows of

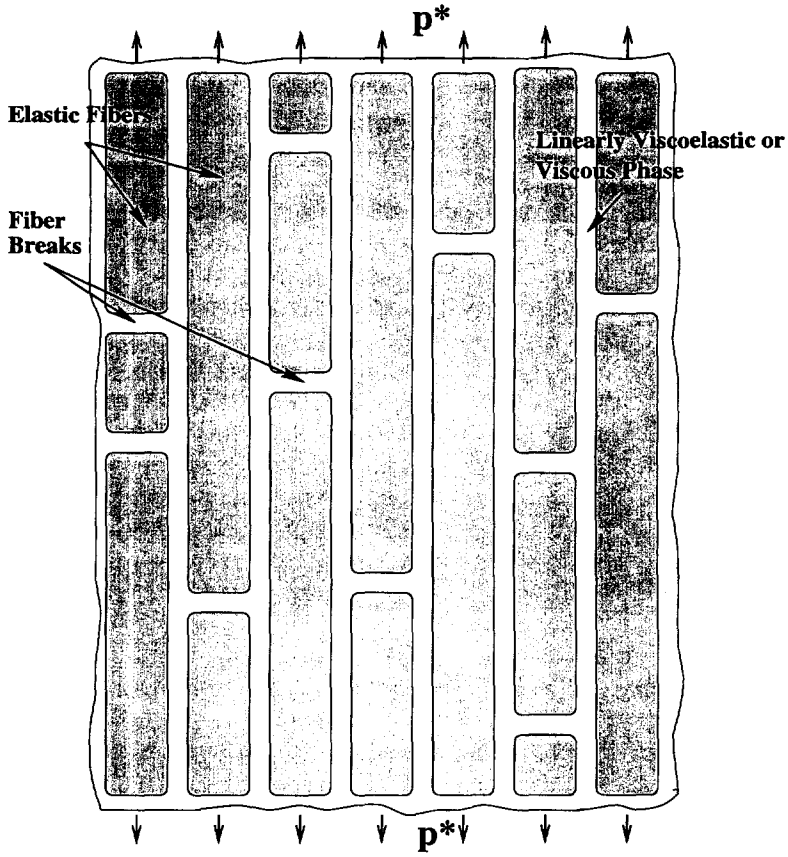

Fig. 1. Planar unidirectional composite microstructure with aligned ceramic fibers or grains embedded in linearly creeping matrix with pre-existing fiber fractures.

transversely aligned breaks (more than 20) in the form of a crack. Even more convincing is the agreement in the axial fiber stress profiles of the elastic (Beyerlein *et al.*, 1996) and elastic/plastic/debond shear-lag model predictions (Beyerlein and Phoenix, 1996) with those of piezospectroscopic measurement techniques (He *et al.*, 1998; Beyerlein *et al.*, 1998).

Predictions from the shear-lag model are most accurate when the fiber volume V_f is relatively high (say 0.4 and above) and the fiber-to-matrix initial modulus ratio is high (i.e. $E_f V_f \gg 2(1+\nu_m)G_m V_m$). However it often gives useful predictions even when this condition is not met, especially when the matrix creep strain dominates the initial elastic strain. Therefore, the most appropriate application of the VBI technique is to fibrous composites having polymer matrices of low volume fraction and at moderate temperatures. Examples are graphite fibers in a thermosetting matrix such as epoxy or a thermoplastic matrix, e.g. polyetheretherketone (PEEK). The model also applies to advanced ceramic materials with highly oriented, fibrous microstructures in a glassy matrix phase, wherein cavitation near grain ends plays the role of fiber breaks.

1.2. *Related modeling attempts in the literature*

Though there exists extensive literature on creep deformation in composites, only a few account for some type of local damage and even fewer are probabilistic treatments. While many neglect the influence of local damage evolution, they do show how variation in microstructural features and time-dependent deformation of one or more distinct phases can influence steady-state creep (Lilholt, 1985; Dragone and Nix, 1990; Onck and Vander Giessen, 1997). Only a few studies develop probabilistic models that account for the effects of initial and subsequent fiber breaks at the microstructural level (Otani *et al.*, 1991; Ibnabdeljalil and Phoenix, 1995; Lee *et al.*, 1996). Some others have focused on micromechanical stress analyses involving creeping matrices but for composites consisting of

either a small number of fibers or containing only one break or a small cluster (Lifshitz and Rotem, 1970; Gusev and Ovchinskii, 1984, Lagoudas *et al.*, 1989; Mason *et al.*, 1992; Stumpf and Schwartz, 1993). Several works focus on detailed calculations of the deformation around one break in a single fiber either analytically (Du and McMeeking, 1995), using shear-lag (Lifshitz and Rotem, 1970; Gusev and Ovchinskii, 1984), or using finite element analysis (Dragone and Nix, 1990; Song *et al.*, 1995), mostly for use in unit cell or global load sharing models.

Despite restrictions on composite or "damage zone" size and shape, the works cited above have provided considerably physical insight into local stress redistribution. All show that an important consequence of matrix creep, whether power-law in time (Lifshitz and Rotem, 1970; Lagoudas *et al.*, 1989) or power-law in stress (Du and McMeeking, 1995; Iyengar and Curtin, 1997) is broadening of the "ineffective" length surrounding a break over which the fiber recovers the far field stress. Also this broadening is approximately proportional to the square root of the matrix creep compliance. As Lagoudas *et al.* (1989) further demonstrated, this leads to growing effective load transfer or overload lengths on neighboring fibers, also scaling with the square-root of compliance. For one to five aligned breaks, they also showed that the location and magnitude of peak stress concentrations on neighboring intact fibers were time-independent and equivalent to the corresponding values from the elastic Hedgepeth (1961) solution. We show that similar features prevail for larger cracks, containing up to 20 times more fiber breaks. But for arbitrarily spaced and non-aligned breaks, the peak stresses on neighboring fibers are time-dependent, the reason being that the time-growing overload regions from non-aligned and widely spaced fiber breaks will eventually interact causing more load to be transferred to the surrounding intact material. Furthermore, over a time scale that depends on actual size and spacing of the breaks, the local creep can accelerate to become roughly proportional to the creep compliance itself (rather than the square-root).

All these effects are important in ultimately tackling the problem of predicting the primary and secondary creep response, where and when successive breaks statistically occur, and when and where localized, catastrophic instability emerges in the tertiary stage. Apart from developing the VBI technique, the objective of the present work is to study the important characteristics of how fiber and matrix stresses redistribute in time due solely to matrix creep, and how this evolution can lead to new (delayed) fiber breaks. For demonstration purposes, the VBI technique is applied to several highly structured spatial descriptions of fiber breaks.

Lastly we mention analyses for related problems in the fluid mechanics literature involving a three-dimensional suspension of aligned, slender rigid particles in a Newtonian viscous fluid (Batchelor, 1971; Goddard, 1976; Harlen and Koch, 1992). Such work applies to extrusion and injection molding of discontinuous fiber composites (Pipes *et al.*, 1991, 1992). Interest is typically in calculating the extensional viscosity of the suspension and average tensile stress contribution of the elongated particles under quasi-steady state flows, semidilute conditions and shear dominated flow near an isolated particle (used as a unit cell) or between close particles in simple arrays.

Unfortunately, these powerful analyses have two drawbacks that severely limit their use. First, the elasticity of the particles is completely neglected. This means that the transient deformation behavior so important to the evolving stress redistribution around the fiber discontinuities, is lost completely. Second, mean field, steady-state assumptions for single particles cannot be made "*a priori*" if one wishes to address the following key issues: the roles played by microstructural length scales, evolving local stress redistribution, fiber failure statistics, and ultimate damage localization and stress-rupture. The VBI technique deals directly with these complications, though at the expense of some simplifications in the mechanics and geometry.

2. MODEL FORMULATION

2.1. *Composite lamina*

The basic shear-lag model is illustrated in Fig. 2, which shows the central region within an infinite, two-dimensional lamina of evenly spaced fibers and matrix bays together with

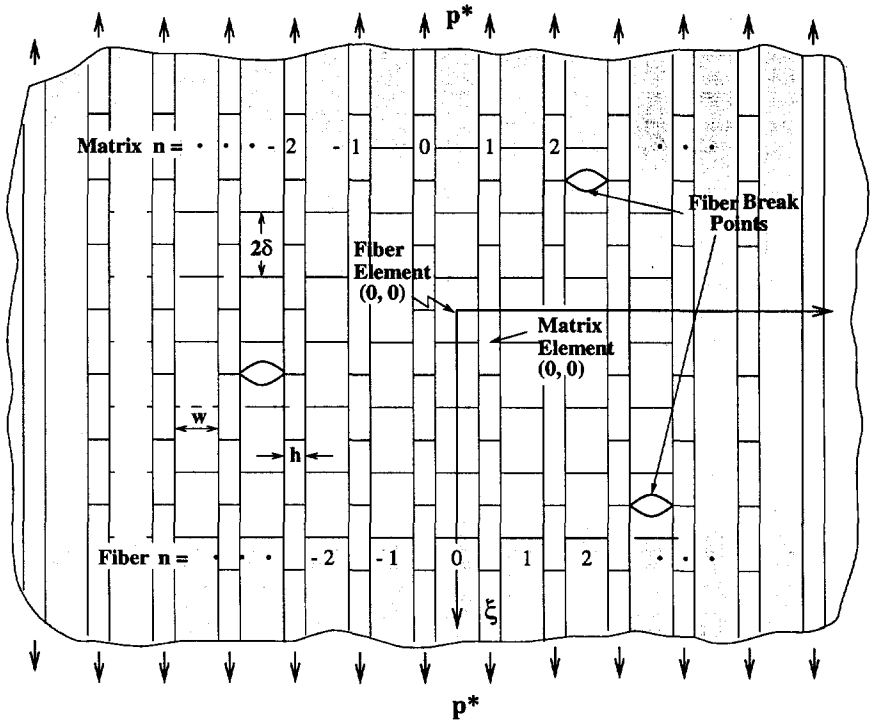

Fig. 2. Discretized region in planar fiber composite showing address scheme for fiber elements, matrix elements, and breaks.

a few, arbitrarily placed, fiber break points. Though the basic shear-lag solutions are analytical, a brick-like discretization scheme is used to establish a fine mesh of spatial points at which to calculate and plot stresses and displacements, and to locate fiber breaks. The center fiber is numbered $n = 0$, the fibers to the right are numbered $n = 1, 2, \ldots, \infty$ and those to the left, $n = -1, -2, \ldots, -\infty$. The matrix bay to the right of fiber n is matrix bay n. Likewise, in the longitudinal direction, the fiber and matrix elements are numbered in the positive direction from $(n, m = 0)$ to $(n, m = \infty)$, and in the negative direction, from $(n, m = -1)$ to $(n, m = -\infty)$. Also indicated on Fig. 2 is w, the matrix width, and h, the fiber diameter. We also take h to be the lamina thickness. For the fibers, E is the Young's modulus, and A is the fiber cross-sectional area. For the matrix, $J(\mathscr{T})$ is the creep function of the matrix in terms of actual time $\mathscr{T}$. The symbol t is reserved for normalized time in which most of the analysis is framed.

The matrix is linearly viscoelastic in shear following a power law creep function $J(\mathscr{T})$, which takes one of two possible forms:

$$J_1(\mathscr{T}) = J_e(1 + \mathscr{T}/\mathscr{T}_c)^{\alpha}, \tag{1}$$

if its initial elastic response is to be modeled explicitly, as in Lagoudas *et al.* (1989), and

$$J_0(\mathscr{T}) = J_e(\mathscr{T}/\mathscr{T}_c)^{\alpha}, \tag{2}$$

if initial elastic effects are to be ignored. The positive constant $\mathscr{T}_c$ is the characteristic time constant for matrix relaxation, the nonnegative parameter α is called the creep exponent, and in (1) the positive constant J_e is the elastic compliance with dimensions [stress^{-1}]. Also J_e and $\mathscr{T}_c$ are not really independent parameters, and for a particular material, α, J_e, and $\mathscr{T}_c$ in $J(\mathscr{T})$ (1) may depend on temperature and stress level.

Most of the analysis will concentrate on model (2), which retains the parameter structure of (1) because later we find that a good approximation of the initial elastic

response is obtained by setting $\mathscr{T}/\mathscr{T}_c = 1$ in the results. Solutions under (2) will be valid for times beyond the short, transient time period of order $\mathscr{T}_c$. Also for phenomenological reasons we restrict our attention to α in the range $0 \leqslant \alpha \leqslant 1$. In one extreme, $\alpha = 0$, the matrix is linearly elastic in shear and at the other, $\alpha = 1$, the matrix is Newtonian viscous in shear. The creep compliance (2) then reduces to

$$J_0(\mathscr{T}) = \mathscr{T}/\eta \tag{3a}$$

where

$$\eta = \mathscr{T}_c/J_e \tag{3b}$$

is the shear viscosity given in terms of parameters in (2). The power law form (1) reproduces well creep curves for a number of different materials, in which α typically varies from 0.02–0.4 for epoxies and plastics, but could also be 0.5 or more, such as in some polyesters (Rabotnov, 1969; Lifshitz and Rotem, 1970). For the remainder of the work, we will refer to the matrix deformation as linearly elastic when $\alpha = 0$, linearly viscoelastic when $0 < \alpha < 1$, and linearly viscous when $\alpha = 1$.

Under the creep law (1), the range $0 < \alpha \ll 1$ was studied by Lagoudas *et al.* (1989) who gave some closed-form results, and showed that fiber stress concentrations disperse around breaks according to $\mathscr{T}^{\alpha/2}$ with plots given by $\alpha \leqslant 0.3$. While the basic character of their results and scaling for large times are largely correct, there is a small error in their analysis since in the limit as $t \to 0$, the resulting solutions fail to collapse as they should to the elastic shear-lag solutions of Hedgepeth (1961). Thus, for the solutions later derived under (2), we will make appropriate connection to Hedgepeth's elastic results through taking the appropriate limits as $\alpha \to 0$.

2.2. *Shear-lag equations and normalized variables*

Let $p_n(x, \mathscr{T})$ and $u_n(x, \mathscr{T})$ be the tensile force and displacement, respectively, in fiber n at location x and time t, and let $\tau_n(x, \mathscr{T})$ be the effective shear stress in matrix bay n. First consider the equilibrium of a fiber element of length ∂x in fiber n. According to shear-lag assumptions, the axial gradient in the fiber tensile force is related to the difference between the surface shear tractions applied by the two adjacent matrix bays $(n-1)$ and n. From the theory of linear viscoelasticity, the current matrix shear stress $\tau_n(x, \mathscr{T})$ is determined from the entire strain history of the matrix, $\gamma_n(x, \mathscr{T}')$ for $-\infty < \mathscr{T}' \leqslant \mathscr{T}$. Assuming the fiber and matrix are perfectly bonded, the shear strain $\gamma_n(x, \mathscr{T})$ in matrix bay n at time $\mathscr{T}$ is $\gamma_n(x, \mathscr{T}) = \{u_{n+1}(x, \mathscr{T}) - u_n(x, \mathscr{T})\}/w$. Lastly, applying Hooke's law to the fibers, one obtains the basic equation for $u_n(x, \mathscr{T})$.

The next step is to introduce normalizations that will render the length and time scales and the time-dependent stress and displacements dimensionless. As in Lagoudas *et al.* (1989), the normalizations for the fiber axial coordinate x and time $\mathscr{T}$, respectively,

$$\xi = \frac{x}{\sqrt{\dfrac{wEAJ_e}{h}}}, \tag{4}$$

and

$$t = (\mathscr{T}/\mathscr{T}_c). \tag{5}$$

Also, the normalized relaxation modulus $\mathscr{G}(t)$ is

$$\mathscr{G}(t) = G(\mathscr{T}_c t)/G_e, \tag{6a}$$

and the creep compliance $\mathscr{J}(t)$ is

$$\mathcal{J}(t) = J(\mathcal{T}_c t)/J_e, \tag{6b}$$

with subscripts added for $J_0(\mathcal{T})$ of (2) or $J_1(\mathcal{T})$ of (1). G_e is the elastic shear modulus for the matrix with inverse J_e, the instantaneous shear compliance in (1). Under a constant tensile load p^* per fiber, applied at $x = \pm\infty$ for $t > 0$, the normalized fiber displacements $U_n(\xi, t)$ and loads $P_n(\xi, t)$ are

$$U_n(\xi, t) = \frac{u_n(x, \mathcal{T})}{p^* \sqrt{\dfrac{wJ_e}{AhE}}} \tag{7}$$

and

$$P_n(\xi, t) = \frac{p_n(x, \mathcal{T})}{p^*}. \tag{8}$$

The normalized, dimensionless versions of the matrix shear stresses, $T_n(\xi, t)$, strains, $\Gamma_n(\xi, t)$, and strain rate, $\partial\Gamma_n(\xi, t)/\partial t$, are

$$T_n(\xi, t) = \frac{\tau_n(x, \mathcal{T})\sqrt{EAhwJ_e}}{p^*}, \tag{9}$$

$$\begin{aligned}\Gamma_n(\xi, t) &= \frac{\gamma_n(x, \mathcal{T})}{p^*}\sqrt{\frac{EAhw}{J_e}} \\ &= U_{n+1}(\xi, t) - U_n(\xi, t),\end{aligned} \tag{10}$$

and

$$\partial\Gamma_n(\xi, t)/\partial t = \frac{\{\partial\gamma_n(x, \mathcal{T})/\partial\mathcal{T}\}\mathcal{T}_c}{p^*}\sqrt{\frac{EAhw}{J_e}}. \tag{11}$$

Applying normalizations (4), (7), and (8), the normalized fiber axial load (or stress) and strain are related by

$$P_n(\xi, t) = \frac{\partial U_n(\xi, t)}{\partial\xi}. \tag{12}$$

Using the normalizations (4), (5), and (6a) as well as (9)–(11), the constitutive relation for the matrix becomes

$$T_n(\xi, t) = \int_{-\infty}^{t} \mathcal{G}(t - t')\{\partial\Gamma_n(\xi, t')/\partial t'\}\,\mathrm{d}t. \tag{13}$$

Lastly, applying the above normalizations, the fundamental shear-lag equation for $u_n(x, \mathcal{T})$ becomes

$$\frac{\partial^2 U_n(\xi, t)}{\partial\xi^2} + \int_{-\infty}^{t} \mathcal{G}(t - t')\frac{\partial}{\partial t'}\{U_{n+1}(\xi, t') - 2U_n(\xi, t') + U_{n-1}(\xi, t')\}\,\mathrm{d}t' = 0, \tag{14}$$

where t' is a normalized integration variable.

In dimensional variables, the boundary conditions are a constant load per fiber p^* applied at $x = \pm\infty$, and the fiber loads are zero at the fiber break sites say (x_1, n_1), (x_2, n_2), $(x_3, n_3), \ldots$. In normalized variables, this corresponds to $\partial U_n(\xi, t)/\partial\xi = 1$ at $\xi = \pm\infty$ and $\partial U_n(\xi, t)/\partial\xi = 0$ at (ξ_1, n_1), (ξ_2, n_2), $(\xi_3, n_3), \ldots$. These boundary conditions are more general than those in Lagoudas *et al.* (1989), who considered a symmetric row of breaks along the $\xi = 0$ plane, where they specified $U_n(0, t) = 0$ for unbroken fibers. In extending the formulation to an arbitrary 2-D array of fiber breaks, the latter assumption is untrue, and $U_n(\xi, t)$ must be obtained from the solution.

Results from the elastic analyses show that the characteristic fiber distance l_c, corresponding to $\xi = 1$, is also the characteristic elastic load transfer length, or the longitudinal distance from the break plane over which an immediately adjacent fiber is overloaded. (The total overload length is double this value.) As we show later, the corresponding time-dependent load transfer length begins to grow beyond the elastic l_c when $t > 1$. Referring back to Fig. 2, each fiber and matrix element in the grid is of length 2δ, where δ is a normalized distance. To obtain sufficient resolution in the numerical computations, $\delta = 1/10$, or in terms of dimensional variables, $d = (1/10)\sqrt{wEAJ_e/h}$, as in previous elastic shear-lag analyses (Beyerlein *et al.*, 1996). Since ξ in the elastic shear-lag problem is identical to (4) upon taking $G_e = 1/J_e$, d is one-tenth of l_c.

2.3. *Laplace transforms*

The first step in solving (14) is to take its Laplace transform, which yields

$$\frac{\partial^2 \underline{\mathscr{U}}_n(\xi, s)}{\partial\xi^2} + s\underline{\mathscr{G}}(s)\{\underline{\mathscr{U}}_{n+1}(\xi, s) - 2\underline{\mathscr{U}}_n(\xi, s) + \underline{\mathscr{U}}_{n-1}(\xi, s)\} = 0, \tag{15}$$

where underscoring of a variable denotes it Laplace transform, and s is the normalized Laplace transform variable. As in Lagoudas *et al.* (1989) the Laplace transform, $\underline{\mathscr{J}}_1(s)$, of the normalized version of the creep function (1), given by (6b), is easily found to be

$$s\underline{\mathscr{J}}_1(s) = \frac{s^\alpha + \Gamma(1+\alpha)}{s^\alpha}, \quad 0 \leqslant \alpha, \tag{16}$$

and for (2) it reduces to

$$s\underline{\mathscr{J}}_0(s) = \frac{\Gamma(1+\alpha)}{s^\alpha}, \quad 0 \leqslant \alpha, \tag{17}$$

where $\Gamma(\cdot)$ is the gamma function. A well-known relationship (Christensen, 1982) between the Laplace transforms of the creep compliance $\underline{J}(s)$ and the relaxation modulus $\underline{\mathscr{G}}(s)$ is

$$s\underline{\mathscr{G}}(s) = \frac{1}{s\underline{\mathscr{J}}(s)}, \tag{18}$$

from which we immediately get the corresponding transform $s\underline{\mathscr{G}}(s)$ for $\mathscr{G}(t)$. Conveniently, the form of the solutions to $U_n(\xi, t)$, $P_n(\xi, t)$, $T_n(\xi, t)$ and $\Gamma_n(\xi, t)$ in normalized variables depends only on one material parameter, α.

3. ISOLATED FIBER BREAK SOLUTION

3.1. *Formulation and Laplace transforms*

The first task in the VBI technique is to solve the problem of an isolated fiber break in an infinite lamina under the special conditions of zero load applied in the far field and a unit normalized compressive load applied to the fiber break ends. To distinguish this auxiliary solutions under zero far field load from the final solution under a constant far

field load (and no load at the breaks), we use the symbols V_n and L_n instead of U_n and P_n, for the normalized fiber tensile displacement and load, respectively. Furthermore, to distinguish the isolated break (unit) solution from the general auxiliary solution, we use superscript "u", i.e., V_n^u, L_n^u, T_n^u, and Γ_n^u instead of V_n, L_n, T_n and Γ_n for the normalized fiber tensile displacement and load, and the matrix shear stress and strain, respectively.

At $t = 0^+$, a compressive load of unit magnitude is suddenly applied to the isolated break in fiber $n = 0$ at $\xi = 0$, and is maintained for $t \geqslant 0$, and at $\xi = \pm\infty$, the load is zero. So for $t \geqslant 0$, the boundary conditions are

$$L_n^u(0, t) = \frac{\partial V_n^u(0, t)}{\partial \xi} = -1 \quad \text{at } n = 0 \quad \text{and} \quad t > 0, \tag{19a}$$

and

$$L_n^u(\pm\infty, t) = \frac{\partial V_n^u(\pm\infty, t)}{\partial \xi} = 0, \quad \text{for all } n \quad \text{and} \quad t \geqslant 0, \tag{19b}$$

where in the above, we have used (12). Also, since the fiber displacements are anti-symmetric about the plane $\xi = 0$, we have

$$V_n^u(0, t) = 0, \quad |n| > 0 \quad \text{and} \quad t \geqslant 0. \tag{19c}$$

The technique of solution for the isolated fiber break problem is given in Lagoudas *et al.* (1989) and involves first taking Laplace transforms of (14) (with V_n^u in place of U_n) subject to the boundary conditions (19), and then applying a discrete Fourier transform on n. For an isolated break, the resulting expression for the fiber displacements is (in terms of Laplace inversion)

$$V_n^u(\xi, t) = \operatorname{sgn}(\xi)\frac{1}{4}\int_0^{\pi} \cos(n\theta) \times \mathbf{L}^{-1}\left[\frac{1}{s\sqrt{s\underline{\mathscr{G}}(s)}}\exp\{-2|\xi|\sin(\theta/2)\sqrt{s\underline{\mathscr{G}}(s)}\}\right]\mathrm{d}\theta, \tag{20}$$

where "$\mathbf{L}$" is the Laplace operator. Similarly, expressions for the fiber loads and matrix shear strains are

$$L_n^u(\xi, t) = -\frac{1}{2}\int_0^{\pi} \cos(n\theta)\sin(\theta/2) \times \mathbf{L}^{-1}\left[\frac{1}{s}\exp\{-2|\xi|\sin(\theta/2)\sqrt{s\underline{\mathscr{G}}(s)}\}\right]\mathrm{d}\theta, \tag{21}$$

and using (10)

$$\Gamma_n^u(\xi, t) = V_{n+1}^u(\xi, t) - V_n^u(\xi, t). \tag{22}$$

By (10), (13) (with V_n^u replacing U_n), and (22), the matrix shear stresses are

$$T_n^u(\xi, t) = \operatorname{sgn}(\xi)\frac{1}{4}\int_0^{\pi} [\cos((n+1)\theta) - \cos(n\theta)] \times \mathbf{L}^{-1}\left[\frac{\sqrt{s\underline{\mathscr{G}}(s)}}{s}\exp\{-2|\xi|\sin(\theta/2)\sqrt{s\underline{\mathscr{G}}(s)}\}\right]\mathrm{d}\theta \tag{23}$$

where $\operatorname{sgn}(\xi) = 1$ for $\xi \geqslant 0$ and $\operatorname{sgn}(\xi) = -1$ for $\xi < 0$. In the present work, we use $\mathscr{J}_0(t)$ given by (2), with the corresponding normalized relation modulus being $\mathscr{G}_0(t)$. The Laplace transform $s\underline{\mathscr{G}}_0(s)$ is given by (18) and (17) for substitution into (20)–(23).

Our intent is to model a wide variety of polymeric materials, which exhibit various flow behavior, for values of α ranging from 0–1, and glassy matrix phases in ceramics which exhibit viscous deformations, $\alpha = 1$. We begin with the latter case, which yields certain simplifications and a special mathematical structure as compared to the case $0 \leqslant \alpha < 1$.

3.2. *Case I* ($\alpha = 1$)

In this case (3) applies, as the matrix is Newtonian viscous in shear, so $J_0(\mathscr{T}) = \eta^{-1}\mathscr{T}$, and

$$\tau_n(x, \mathscr{T}) = \eta\, \partial\gamma_n(x, \mathscr{T})/\partial\mathscr{T}. \tag{24}$$

The corresponding relaxation modulus is

$$G_0(\mathscr{T}) = \eta\delta(\mathscr{T}), \tag{25}$$

where $\delta(\mathscr{T})$ is the Dirac delta function with dimensions [time^{-1}]. The normalized time scale given by (5) reduces to,

$$t = \frac{\mathscr{T}}{\mathscr{T}_c} = \frac{\mathscr{T}}{\eta J_e}, \quad (\alpha = 1). \tag{26}$$

Substituting (26) into (11), the matrix strain rate reduces to

$$\partial\Gamma_n(\xi, t)/\partial t = \frac{\{\partial\gamma_n(x, \mathscr{T})/\partial\mathscr{T}\}\eta\sqrt{J_e EAhw}}{p^*}, \quad (\alpha = 1). \tag{27}$$

Starting with the general form (20), we derive the exact, closed form solution for $V_n^u(\xi, t)$ in Appendix A, which is

$$V_n^u(\xi, t)/\sqrt{t} = \mathscr{V}_n(z)$$
$$= \operatorname{sgn}(z)\frac{1}{2}\int_0^\pi \cos(n\theta)\left\{\frac{1}{\sqrt{\pi}}\exp(-C_\theta^2|z|^2) - C_\theta|z|\operatorname{erfc}(C_\theta|z|)\right\}\mathrm{d}\theta \tag{28}$$

where

$$C_\theta = \sin(\theta/2), \tag{29}$$

and z is the similarity variable,

$$z = \frac{\xi}{\sqrt{t}}. \tag{30}$$

The corresponding tensile load $L_n^u(\xi, t) = \partial V_n^u(\xi, t)/\partial\xi$ is

$$L_n^u(\xi, t) = \mathscr{L}_n(z)$$
$$= -\frac{1}{2}\int_0^\pi C_\theta \cos(n\theta)\operatorname{erfc}(C_\theta|z|)\,\mathrm{d}\theta. \tag{31}$$

From (13) and (25), the matrix shear stress, $T_n^u(\xi, t)$, and the strain rate, $\partial\Gamma_n^u(\xi, t)/\partial t$, are related by

$$T_n^u(\xi, t) = \frac{\partial \Gamma_n^u(\xi, t)}{\partial t}, \quad (\alpha = 1) \tag{32}$$

where from (28), $\Gamma_n^u(\xi, t)$ is

$$\Gamma_n^u(\xi, t) = V_{n+1}^u(\xi, t) - V_n^u(\xi, t) = \sqrt{t}\{\mathscr{V}_{n+1}(z) - \mathscr{V}_n\}, \quad (\alpha = 1). \tag{33}$$

Substituting (28) into (13) and the result into (32) yields for $T_n^u(\xi, t)$

$$\sqrt{t}T_n^u(\xi, t) = \mathscr{T}_n(z)$$
$$= \operatorname{sgn}(z)\frac{1}{4\sqrt{\pi}}\int_0^{\pi} [\cos((n+1)\theta) - \cos(n\theta)]\exp(-C_\theta^2|z|^2)\,\mathrm{d}\theta. \tag{34}$$

Notably all these single break solutions can be defined as functions of the similarity variable z only. Significantly z couples the two independent variables, time and distance, into one. In later methods for solving the multiple fiber break problem, this similarity structure will lead to significant savings in computation time and effort, and also simplify understanding the relationships between microstructural length scales and time-to-rupture in model systems. In fact this similarity structure (and exact result) is a beneficial artifact of considering only the time-dependent response of the matrix or considering (2) rather than (1). For instance, these unit solutions have a much simpler form than the corresponding approximate expressions obtained by Lagoudas *et al.* (1989), using (1) for the matrix compliance. From their results, effects of the initial elastic component appear to be very small.

It is interesting to note that (31) can be obtained by applying the variable transformation z to the stress formulation of the equilibrium eqn (14), which is

$$\frac{\partial^2 L_n^u(\xi, t)}{\partial \xi^2} + \frac{\partial}{\partial t}\{L_{n+1}^u(\xi, t) - 2L_n^u(\xi, t) + L_{n-1}^u(\xi, t) = 0. \tag{35a}$$

Using the similarity variable, $z = \xi/\sqrt{t}$, and the structure $L_n^u(\xi, t) = \mathscr{L}_n(z)$, the above partial differential equation transforms to an ordinary differential equation in $\mathscr{L}_n(z)$, namely

$$\frac{\mathrm{d}^2\mathscr{L}_n(z)}{\mathrm{d}z^2} + \frac{z}{2}\frac{\mathrm{d}}{\mathrm{d}z}[\mathscr{L}_{n+1}(z) - 2\mathscr{L}_n(z) + \mathscr{L}_{n-1}(z)] = 0. \tag{35b}$$

In Appendix A, we use discrete Fourier transforms on (35b) to obtain the same solution for $\mathscr{L}_n(z)$ as in (31), without using Laplace transforms.

3.3. *Case II* ($0 < \alpha < 1$)

The primary difference between the cases $\alpha = 1$ and $0 < \alpha < 1$ is that the fiber L_n^u and V_n^u, and the matrix T_n^u and Γ_n^u are dependent on the deformation history for $0 < \alpha < 1$. For arbitrary α, the Laplace inversions needed in (20)–(23) are given in Appendix B. Substituting results in Appendix B into (20)–(23) yields

$$L_n^u(\xi, t) = \mathscr{L}_n(z)$$
$$= -\frac{1}{\pi\alpha}\int_0^{\pi} \cos(n\theta)C_\theta \int_0^{\infty} [\exp\{-\hat{a}\cos(\pi\alpha/2)|z|v\}]$$
$$\times \sin\{\hat{a}\sin(\pi\alpha/2)|z|v\}\frac{1-\exp(-v^{2/\alpha})}{v}\mathrm{d}v\,\mathrm{d}\theta, \tag{36}$$

$$V_n^u(\xi, t)/t^{\alpha/2} = \mathscr{V}_n(z)$$

$$= \operatorname{sgn}(z)\frac{\sqrt{\Gamma(\alpha+1)}}{2\pi\alpha}\int_0^{\pi}\cos(n\theta)\int_0^{\infty}[\exp\{-\hat{a}\cos(\pi\alpha/2)|z|v\}]$$

$$\times\sin\{\hat{a}\sin(\pi\alpha/2)|z|v+\pi\alpha/2\}\frac{1-\exp(-v^{2/\alpha})}{v^2}\,dv\,d\theta, \tag{37}$$

$$t^{\alpha/2}T_n^u(\xi, t) = \mathscr{T}_n(z)$$

$$= -\operatorname{sgn}(z)\frac{1}{2\pi\alpha\sqrt{\Gamma(\alpha+1)}}\int_0^{\pi}[\cos((n+1)\theta)-\cos(n\theta)]$$

$$\times\int_0^{\infty}\sin\{\hat{a}\sin(\pi\alpha/2)|z|v-\pi\alpha/2\}$$

$$\times[\exp\{-\hat{a}\cos(\pi\alpha/2)|z|v-v^{2/\alpha}\}]\,dv\,d\theta, \tag{38}$$

and by (10)

$$\Gamma_n^u(\xi, t) = t^{\alpha/2}\{\mathscr{V}_{n+1}(z)-\mathscr{V}_n(z)\}, \tag{39}$$

where

$$\hat{a} = 2C_\theta/\sqrt{\Gamma(\alpha+1)}, \tag{40}$$

with $C_\theta = \sin(\theta/2)$ as before, and now

$$z = \frac{\xi}{t^{\alpha/2}}. \tag{41}$$

So the solutions are again in terms of the similarity variable z.

3.4. *The case* $\alpha = 0$ *and approximations for Case II*

Turning to useful approximations, Schapery's direct method for approximate Laplace inversion of a given function, say $\underline{\vartheta}(s)$, is

$$\vartheta(t) = s\underline{\vartheta}(s)\,|_{s=\exp(-\gamma)/t} \tag{42}$$

where γ is Euler's constant, $\gamma \cong 0.5772$. Equation (42) is appropriate for the range of s where a plot of $s\underline{\vartheta}(s)$ vs $\log(s)$ has small curvature and is exact when $s\underline{\vartheta}(s)$ is linear in $\log(s)$ (Schapery, 1967). (If, in fact, $\log[s\underline{\vartheta}(s)]$ vs $\log(s)$ satisfies the small curvature condition, Schapery advises using 0.5 in place of $\exp(-\gamma)$, but in our case, this alteration makes little difference.) In our case, small curvature in the various functions, L_n^u, V_n^u, T_n^u and Γ_n^u [when in the Laplace form $s\underline{\vartheta}(s)$] over the entire range of s, n, and ξ is subjectively associated with $\alpha \leqslant 0.5$.

We find that applying Schapery's direct inversion method (42)–(20)–(23) yields approximations that have the same shape as the elastic results of Hedgepeth (1961). First we present Hedgepeth's results for load, displacement, shear stress, and shear strain, respectively, as

$$L_n^{u,e}(\xi) = -\frac{1}{2}\int_0^{\pi} \cos(n\theta) C_\theta \exp(-2C_\theta|\xi|)\,\mathrm{d}\theta, \tag{43}$$

$$V_n^{u,e}(\xi) = \mathrm{sgn}(\xi)\frac{1}{4}\int_0^{\pi} \cos(n\theta)\exp(-2C_\theta|\xi|)\,\mathrm{d}\theta, \tag{44}$$

and

$$\begin{aligned}\Gamma_n^{u,e}(\xi) &= T_n^{u,e}(\xi)\\ &= \mathrm{sgn}(\xi)\frac{1}{4}\int_0^{\pi} [\cos((n+1)\theta)-\cos(n\theta)]\exp(-2C_\theta|\xi|)\,\mathrm{d}\theta,\end{aligned} \tag{45}$$

where, ξ is (4) with $G_e = 1/J_e$. Schapery's direct inversion method yields

$$L_n^u(\xi, t) = \mathscr{L}_{n+1}(z) \approx L_n^{u,e}(\beta_s\xi/t^{\alpha/2}), \tag{46}$$

$$V_n^u(\xi, t) = t^{\alpha/2}\mathscr{V}_{n+1}(z) \approx (t^{\alpha/2}/\beta_s)V_n^{u,e}(\beta_s\xi/t^{\alpha/2}), \tag{47}$$

and

$$T_n^u(\xi, t) = \mathscr{T}_{n+1}(z)/t^{\alpha/2} \approx \beta_s t^{-\alpha/2} T_n^{u,e}(\beta_s\xi/t^{\alpha/2}) \approx \Gamma_n^u(\xi, t), \tag{48}$$

where the parameter β_s is

$$\beta_s = \exp(-\gamma\alpha/2)/\sqrt{\Gamma(\alpha+1)}, \tag{49}$$

and ranges from 1.00–0.7493 as α increases from 0–1. In fact, these results correspond to the case $\alpha = 0$ as we show in Appendix B upon taking the limit $\alpha \to 0$ in (36)–(41), wherein z reduces simply to ξ.

In Appendix B, we give expansions of the inner second integral of $L_n^u(\xi, t)$, $V_n^u(\xi, t)$, $T_n^u(\xi, t)$, (36)–(38) and here we retain the dominant first and second-order terms (found, respectively, on the first and second lines for each expression below). The approximations are

$$\begin{aligned}L_n^u(\xi, t) &= \mathscr{L}_n(z)\\ &\approx -\frac{1}{2}\int_0^{\pi} \cos(n\theta)C_\theta[\exp\{-2C_\theta\beta_0|z|\}]\,\mathrm{d}\theta\\ &\quad -\kappa_1(\alpha)|z|\int_0^{\pi} \cos(n\theta)C_\theta^2[\exp\{-2C_\theta\beta_0|z|\}]\,\mathrm{d}\theta,\end{aligned} \tag{50}$$

$$\begin{aligned}V_n^u(\xi, t)/t^{\alpha/2} &= \mathscr{V}_n(z)\\ &\approx \mathrm{sgn}(z)\frac{1}{4\beta_0}\int_0^{\pi} \cos(n\theta)\exp\{-2C_\theta\beta_0|z|\}\,\mathrm{d}\theta\\ &\quad -\mathrm{sgn}(z)\kappa_2(\alpha)|z|^2\int_0^{\pi} \cos(n\theta)C_\theta^2[\exp\{-2C_\theta\beta_0|z|\}]\,\mathrm{d}\theta,\end{aligned} \tag{51}$$

and

$$t^{\alpha/2} T_n^u(\xi, t) = \mathscr{T}_n(z)$$

$$\approx -\operatorname{sgn}(z) \frac{1}{4\sqrt{\Gamma(1+\alpha)}} \int_0^\pi [\cos((n+1)\theta) - \cos(n\theta)][\exp\{-2C_\theta \beta_0 |z|\}]\, d\theta$$

$$+ \operatorname{sgn}(z) \kappa_3(\alpha) \int_0^\pi [\cos((n+1)\theta) - \cos(n\theta)]$$

$$\times [1 - 8C_\theta \beta_0 |z|][\exp\{-2C_\theta \beta_0 |z|\}]\, d\theta, \tag{52}$$

where

$$\beta_0 = \Gamma(1+\alpha/2)/\sqrt{\Gamma(1+\alpha)}, \tag{53a}$$

$$\kappa_1(\alpha) = \frac{(\pi\alpha/2)^2}{6} \beta_0, \tag{53b}$$

$$\kappa_2(\alpha) = \frac{(\pi\alpha/2)^2}{12} \beta_0, \tag{53c}$$

and

$$\kappa_3(\alpha) = \frac{(\pi\alpha/2)^2}{24\sqrt{\Gamma(1+\alpha)}}. \tag{53d}$$

As before $\Gamma_n^u(\xi, t) = t^{\alpha/2}(\mathscr{V}_{n+1}(z) - \mathscr{V}_n(z))$.

For small α, the above approximations have a first order structure similar to that obtained by Schapery's direct inversion method, but with β_0 in place of β_s (or with $\Gamma(1+\alpha/2)$ in place of $\exp(-\gamma\alpha/2)$). In fact, $\exp(-\gamma\alpha/2) \approx 1 - \gamma\alpha/2 \approx \Gamma(1+\alpha/2)$, so β_0 and β_s agree up to $O(\alpha^2)$. The next terms are all $O(\alpha^2)$ and are distortions $2C_\theta\beta_0|z|$ or $\{2C_\theta\beta_0|z|\}^2$ of $\exp\{-2C_\theta\beta_0 z\}$. This basic exponential form also arises in elastic solutions upon taking $\alpha = 0$, and thus, for $\alpha = 0$, both Schapery's and our approximations collapse to the corresponding elastic solutions (44)–(46). Also, as we will later see, Schapery's approximations actually work reasonably well even for $\alpha = 1$.

4. MULTIPLE FIBER BREAK SOLUTION

In this section we utilize the isolated break solutions derived in Section 3 to calculate the stress and strain distributions as a function of t around an arbitrary array of fiber breaks. The technique in Lagoudas *et al.* (1989) for transversely aligned breaks is a special case of what follows. In the general case, the main difference (and major complication) is that convolution integrals are introduced to capture the history of the matrix creep deformation around fiber breaks which are misaligned.

4.1. *General time-dependent formulation*

VBI involves calculating load transmission functions, $\Lambda_{ij}(t)$, and solving for weighting functions, $\mathscr{H}_j(t), i,j = 1, \ldots, r(t)$, where $r(t)$ is the number of fiber breaks at time t. For simplicity, we consider the basic case of r preexisting breaks at $t = 0$ and no subsequent breaks over time, so that $r(t) = r$ for $t \geqslant 0$. In Section 4.5 we suggest alterations to treat breaks that occur in time, though more complete analysis is saved for later work.

We define the load transmission function

$$\Lambda_{ij}(t) = L^u_{n_i - n_j}(\xi_i - \xi_j, t) = \mathscr{L}_{n_i - n_j}(z_i - z_j), \tag{54}$$

where $\mathscr{L}_{n_i - n_j}(z_i - z_j)$ is given in Section 3 for the various cases. In other words, $\Lambda_{ij}(t)$ is the

proportion of load transmitted from fiber break j, or single break located at (n_j, ξ_j), to a point (n_i, ξ_i) where break i is located. So for Case I ($\alpha = 1$), $\Lambda_{ij}(t)$ is

$$\Lambda_{ij}(t) = -\frac{1}{2}\int_0^{\pi} \cos\left[(n_i - n_j)\theta\right] \sin(\theta/2)\, \mathrm{erfc}(\sin(\theta/2)|z_i - z_j|)\, \mathrm{d}\theta, \tag{55}$$

and likewise in Case II ($0 < \alpha < 1$) either the exact form (36), approximation (46) or (50) may be used. For all cases, $\Lambda_{ji}(t) = \Lambda_{ij}(t)$ for fixed t, and $\Lambda_{ii}(t) = -1$ (no sum) for all $t \geqslant 0$. The fact that $\Lambda_{ij}(t)$ is a function only of $(n_i - n_j)$ and $(z_i - z_j)$ is the key to simplifying the numerical computations.

In the method, $\Lambda_{ij}(t)$ is multiplied by its corresponding weighting function $\mathscr{K}_j(t)$, which is nonnegative and directly reflects the degree of interaction between fiber break j with all the other fiber breaks (including itself) at time t. Building from the fundamentals of linear viscoelasticity leads to the following system of integral equations for the time-dependent fiber loads, $L_n(\xi, t)$, displacements, $V_n(\xi, t)$ and shear stresses $T_n(\xi, t)$

$$L_n(\xi, t) = \sum_{j=1}^{r}\left[\int_{0^+}^{t} L^u_{n-n_j}(\xi - \xi_j, t-\tau)\frac{\partial \mathscr{K}_j(\tau)}{\partial \tau}\mathrm{d}\tau + L^u_{n-n_j}(\xi - \xi_j, t)\mathscr{K}_j(0^+)\right], \tag{56}$$

$$V_n(\xi, t) = \sum_{j=1}^{r}\left[\int_{0^+}^{t} V^u_{n-n_j}(\xi - \xi_j, t-\tau)\frac{\partial \mathscr{K}_j(\tau)}{\partial \tau}\mathrm{d}\tau + V^u_{n-n_j}(\xi - \xi_j, t)\mathscr{K}_j(0^+)\right], \tag{57}$$

and

$$T_n(\xi, t) = \sum_{j=1}^{r}\left[\int_{0^+}^{t} T^u_{n-n_j}(\xi - \xi_j, t-\tau)\frac{\partial \mathscr{K}_j(\tau)}{\partial \tau}\mathrm{d}\tau + T^u_{n-n_j}(\xi - \xi_j, t)\mathscr{K}_j(0^+)\right], \tag{58}$$

and the shear strain is

$$\Gamma_n(\xi, t) = V_{n+1}(\xi, t) - V_n(\xi, t). \tag{59}$$

In (56), for each break j, if a change in $\mathscr{K}_j(\tau)$ occurs at previous time τ, then load is transferred to fiber point (n, ξ). This additional load is proportional to the change in $\mathscr{K}_j(\tau)$ times the load transmitted from break j over the elapsed time, $t - \tau$. How $\mathscr{K}_j(t)$ changes with time depends on all the break locations, loading history, and in the more general case on times when new, successive fractures occur. Then the total load transmitted to fiber point (n, ξ) at time t from break j is a sum (integral) of all these load contributions occurring at all previous times up to t.

The unknown weighting functions, $\mathscr{K}_j(t)$'s, are solved from the knowledge that the load at each of the r fiber breaks is the prescribed compressive load -1. (Constant break loads imply that the remotely applied load remains constant.) The compressive fiber break load -1 must also equal a sum of the loads transmitted from itself and from the other fiber breaks since application of the load. Using (56) we obtain the following system of integral equations for $\mathscr{K}_1(t), \ldots, \mathscr{K}_r(t)$:

$$-1 = \sum_{j=1}^{r}\left[\int_{0^+}^{t} \Lambda_{ij}(t-\tau)\frac{\partial \mathscr{K}_j(\tau)}{\partial \tau}\mathrm{d}\tau + \Lambda_{ij}(t)\mathscr{K}_j(0^+)\right], \quad i = 1, \ldots, r. \tag{60}$$

Condition (60) says that $\mathscr{K}_j(t)$ and $\Lambda_{ij}(t)$ behave such that for all times t, the break loads remain fixed at -1. Thus the current stress distribution depends on changes in the $\mathscr{K}_j(t)$'s as time progresses and the timescales over which they operate since application of the load at $t = 0^+$.

To solve for the $\mathscr{K}_j(t)$'s we take the Laplace transform of (60) and get

$$\left\{\frac{\mathbf{P}}{s}\right\} = [\underline{\Lambda}(s)s]\{\underline{\mathbf{K}}(s)\}$$

or

$$\{\underline{\mathbf{K}}(s)\} = [\underline{\Lambda}(s)s]^{-1}\left\{\frac{\mathbf{P}}{s}\right\} \tag{61}$$

where $\{\mathbf{P}/s\}$ is an r-dimensional vector whose components are $-1/s$. Solving (61) exactly for $\{\mathbf{K}(t)\}$ requires integration of $[\underline{\Lambda}(s)s]^{-1}$ by use of the Laplace inversion integral formula, which is generally intractable analytically. Thus we will consider approximate and numerical methods of solution.

Finally to calculate the exact solution for a lamina loaded at $\xi = \pm\infty$ by a uniform, unit tensile load $P = 1$ per fiber, a uniform tensile load field $+1$ is superimposed on the above solutions. As a result, all the broken fiber ends will be traction free. The dimensionless fiber loads or stress concentrations, $P_n(\xi, t)$, and fiber displacements, $U_n(\xi, t)$, are, respectively,

$$P_n(\xi, t) = L_n(\xi, t) + 1, \tag{62}$$

and

$$U_n(\xi, t) = V_n(\xi, t) + \xi. \tag{63}$$

The shear stresses and strains, $T_n(\xi, t)$ and $\Gamma_n(\xi, t)$, need no modification.

4.2. *Numerical solution method (Method I)*

Evaluating (56) numerically involves first considering a spanning sequence of suitable discrete times $0^+ = t_0 < t_1 < \cdots < t_k < \cdots < t_p$. To calculate $L_n(\xi, t)$ at (n, ξ) at any time $t > 0$, one considers

$$L_n(\xi, t) = \sum_{j=1}^{r} \{L^u_{n-n_j}(\xi - \xi_j, t)\mathscr{K}_j(0^+) + \sum_{k=1}^{p} L^u_{n-n_j}(\xi - \xi_j, t - t_k)I(t - t_k)[\mathscr{K}_j(t_k) - \mathscr{K}_j(t_{k-1})]\}, \tag{64}$$

where $I(t)$ is the indicator function, namely $I(t) = 1$ for $t \geqslant 0$ and $I(t) = 0$ for $t < 0$. Similar expressions can be obtained for $V_n(\xi, t)$ and $T_n(\xi, t)$ using (57) and (58). Therefore the weighting functions $\mathscr{K}_j(t_k)$, evaluated at the set of points $t_k, k = 0, \ldots, p$ for all r breaks are the solutions to a set of $r(p+1)$ equations. For instance, the $\mathscr{K}_j(t_k)$'s at time t_k are the solutions to set

$$-1 = \sum_{j=1}^{r} \left\{\Lambda_{ij}(t_k)\mathscr{K}_j(0^+) + \sum_{s=1}^{k} \Lambda_{ij}(t_k - t_s)[\mathscr{K}_j(t_s) - \mathscr{K}_j(t_{s-1})]\right\}, \tag{65}$$

where i $= 1, \ldots, r$. Equation (65) can be written compactly as

$$\{\mathbf{C}(t_k)\} = [\Lambda(0^+)]\{\mathbf{K}(t_k)\} \tag{66}$$

where the constant vector $\{\mathbf{C}(t_k)\}$ is known and depends on prior values of $\mathscr{K}_j(t_s)$, $t_0 \leqslant t_s \leqslant t_{k-1}$, through,

$$C_i(t_k) = -1 - \sum_{j=1}^{r} \left\{ \Lambda_{ij}(t_k)\mathscr{K}_j(0^+) + \sum_{s=1}^{k-1} \Lambda_{ij}(t_k - t_s)[\mathscr{K}_j(t_s) - \mathscr{K}_j(t_{s-1})] \right.$$
$$\left. - \Lambda_{ij}(0^+)\mathscr{K}_j(t_{k-1}) \right\}, \quad i = 1, \ldots, r. \tag{67}$$

In (67), $\mathscr{K}_j(t_{-1}) = \mathscr{K}_j(t_0)$, so that $C_i(t_0) = -1$. Thus, $\mathscr{K}_i(t_k)$ must be calculated directly by marching forward in discrete time steps. Knowing the locations of preexisting breaks, we can compute $[\Lambda(0^+)]$ from (56) and (60) and store it at the start. For instance, after calculating the $\mathscr{K}_j(t_s)$'s for $t_0 \leqslant t_s \leqslant t_k$, the fiber load field, $P_n(\xi, t)$, for t in the range, $t_k \leqslant t < t_{k+1}$, is determined using (64) for $L_n(\xi, t)$, followed by (62). Similarly these same $\mathscr{K}_j(t_s)$'s are used to calculate $U_n(\xi, t)$ using discretized versions (57), followed by (63).

In this method, denoted Method I, error enters only through discretization of the convolution (60) and can be minimized by taking small time steps. However, the method can be computationally time consuming for large numbers of breaks and small time steps.

4.3. *Schapery's direct inversion method (Method II)*

A faster approach to solving for $\{\mathbf{K}(t)\}$ in (60) is to employ Schapery's direct Laplace inverse method, (42), which in the current context leads to

$$\{\mathbf{K}(t)\} \approx s\{\underline{\mathbf{K}}(s)\}\,|_{s=\exp(-\gamma)/t} = [\underline{\Lambda}(s)s]^{-1}\{\mathbf{P}\}\,|_{s=\exp(-\gamma)/t} \tag{68}$$

where again $\{\mathbf{P}\}$ is an r-dimensional vector whose components are -1. According to (68), $\{\mathbf{K}(t)\}$ can be approximated by inverting the matrix whose components are approximately,

$$\underline{\Lambda}_{ij}(s)s\,|_{s=\exp(-\gamma)/t} \approx -\frac{1}{2}\int_0^{\pi} \cos[(n_i - n_j)\theta] \sin(\theta/2) \exp[-2\beta \sin(\theta/2)|(z_i - z_j)|]\,\mathrm{d}\theta, \tag{69}$$

and multiplying the result into the vector $\{\mathbf{P}\}$. Thus calculating $\{\mathbf{K}(t)\}$ now becomes straightforward. To be consistent, the fiber loads $L_n(\xi, t)$ and displacements $V_n(\xi, t)$ and matrix shear stresses $T_n(\xi, t)$ are calculated by applying Schapery's approximation to (56)–(58), and using $\{\mathbf{K}(t)\}$ from (68). For instance,

$$L_n(\xi, t) \approx s\underline{L}_n(\xi, s)\,|_{s=\exp(-\gamma)/t}$$
$$= \sum_{j=1}^{r} [s\underline{L}^u_{n-n_j}(\xi - \xi_j, s)s\mathscr{K}_j(s) + s\underline{L}^u_{n-n_j}(\xi - \xi_j, s)\mathscr{K}_j(0^+)]\,|_{s=\exp(-\gamma)/t} \tag{70}$$

where the known functions $s\underline{L}^u_{n-n_j}(\xi - \xi_j, s)$ are

$$s\underline{L}^u_{n-n_j}(\xi - \xi_j, s)\,|_{s=\exp(-\gamma)/t} \approx -\frac{1}{2}\int_0^{\pi} \cos[(n - n_j)\theta] \sin(\theta/2) \exp[-2\beta \sin(\theta/2)|(z - z_j)|]\,\mathrm{d}\theta, \tag{71}$$

and where the $s\underline{\mathscr{K}}_j(s)\,|_{s=\exp(-\gamma)/t}$ are determined from (68). We denote this approximate method as Method II.

Recall from Section 3.4 that Schapery's method is appropriate for the range of s in which a plot of the components of $\{s\underline{\mathbf{K}}(s)\}$ vs $\log(s)$ satisfies the small curvature condition. Subjectively this condition appears to be satisfied over a full range of s (and t). Therefore, the error in using (68) in place of Laplace inversion of (60) will be small in these cases.

4.4. *Method ignoring history (Method III)*

The least accurate approach is simply to solve for $\{\mathbf{K}(t)\}$ based on the current values of $[\Lambda(t)]$, and so the evolving history of $\{\mathbf{K}(t)\}$ is ignored. It tends to be conservative in that the predicted behavior and changes in the components of $\{\mathbf{K}(t)\}$ (which usually increase) will lead the true response. Though this scheme is more crude, it yields a good first approximation of (56)–(60). We call this method, Method III, and note that it is exact when $\{\mathbf{K}(t)\}$ is time-independent, which is the case for a single array of transversely aligned breaks, as studied in Lagoudas *et al.* (1989).

Given time t and r breaks, a system of r equations is solved for the r functions $\mathscr{K}_j(t)$, one associated with each fiber break. The functions are the solutions to the matrix equation

$$\{\mathbf{K}(t)\} = [\Lambda(t)]^{-1}\{\mathbf{P}\} \tag{72}$$

where $\{\mathbf{K}(t)\}$ is the r-dimensional vector of the $\mathscr{K}_j(t)$'s to be solved for, $\{\mathbf{P}\}$ is the r-dimensional vector with entries -1, and $[\Lambda(t)]$ is the $r \times r$ matrix whose components are the influence functions between the fiber breaks evaluated at time t. As in (72), we calculate the fiber and matrix stresses also with no convolution over the history of the weighting functions. Therefore, at any time t, we sum over the current proportions of the loads transmitted from each fiber break j multiplied by its current $\mathscr{K}_j(t)$. Thus, the fiber loads and displacements, and matrix shear stresses become

$$L_n(\xi, t) = \sum_{j=1}^{r} \mathscr{K}_j(t)\mathscr{L}_{n-n_j}(z-z_j), \tag{73}$$

$$V_n(\xi, t) = \sum_{j=1}^{r} \mathscr{K}_j(t)V^u_{n-n_j}(\xi-\xi_j, t), \tag{74}$$

and

$$\Gamma_n(\xi, t) = \sum_{j=1}^{r} \mathscr{K}_j(t)\Gamma^u_{n-n_j}(\xi-\xi_j, t). \tag{75}$$

In Methods II and III, the computation time is dominated by solving for $\{\mathbf{K}(t)\}$ at a given time t, which requires inverting the $r \times r$ matrix in (68) and (72), respectively, where r is the current number of fiber breaks. This is the one advantage Methods II and III have over Method I since they involve no numerical integration. Yet in any one method the calculations are not computationally intensive. Reasons are that first, $\Lambda_{ij}(t)$ is a function of break location i and j and time t through n_i-n_j and z_i-z_j only. Secondly, all the load transmission functions, $\Lambda_{ij}(t)$, for all possible $|n_i-n_j|$ and $|z_i-z_j|$ are integrated numerically at the start and stored. Therefore in using the VBI technique, these values are merely accessed when needed (using an interpolation routine) and subsequent computations for the results to follow take of the order of minutes on a workstation.

4.5. *Fiber breaks in time*

As fiber load profiles change in time near pre-existing fiber breaks, one can expect many successive fiber breaks, especially if the fibers have strengths following Weibull–Poisson statistics. For instance, suppose that at a certain time t'_k, a creep-driven fracture occurs where $k = 1, 2, \ldots$. In Method I, calculating $\{\mathbf{K}(t)\}$ for times $t'_k < t < t'_{k+1}$ still involves summation over the current number of breaks, r', and calculation of all the $\mathscr{K}_j(t')$'s, $j = r_0, \ldots, r'$, up to t by marching forward in discrete time steps. However, the weighting function associated with the delayed fracture $\mathscr{K}_{r'}(t)$ only enters into the calculation for times $t \geqslant t'_k$, i.e. $\mathscr{K}_{r'}(t) = 0$ for $t < t'_k$. In addition, the single fiber load transmission function accounts for the time shift and is taken as $\Lambda_{r'j}(t-t'_k)$. At time t'_k, the dimensions of the matrix systems (68) and (72), in Methods II and III, respectively, increase by one, i.e. $r(t'_k) = r(t'_{k-1})+1 = r'$, where $r(0) = r_0$, the initial number of breaks. Then the weighting

functions are recalculated. In Method III, the past history is ignored, so all breaks which have occurred by time t, are treated as though they all happened at time zero. However, results from a successive break study for aligned breaks in Lagoudas *et al.* (1989) suggest that for $\alpha \ll 1$, Method III can provide a good first approximation.

5. RESULTS

5.1. *Stresses around an isolated break*

Figure 3(a) and (b) compare the normalized fiber tensile stress $P_n(\xi, t) = L_n^u(\xi, t) + 1$ using (46) for $0 < \alpha < 1$ vs the normalized similarity variable $\beta\xi/t^{\alpha/2}$ (dashed line) and $P_n(\xi, t)$ using (31) for $\alpha = 1$ vs $\xi/\sqrt{t}$ (solid line), in the single broken fiber $n = 0$ and for the first intact fiber $n = 1$, respectively. [Here β may represent either β_s (49) or β_0 (53a).] In these cases, a plot of $P_n(\xi, t)$ vs ξ would show self-similar growth in the overload region. The case $\alpha = 0$ (also dashed) corresponds to the elastic isolated break solution

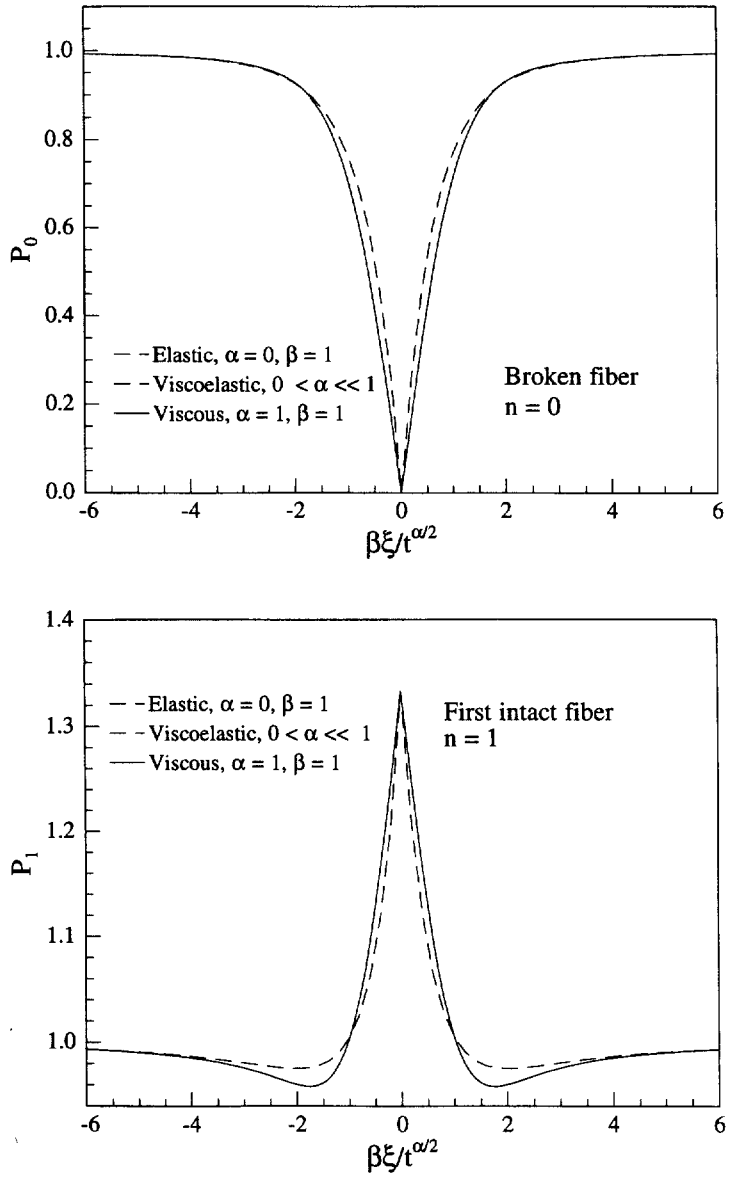

Fig. 3. Normalized fiber tensile load profiles showing stress concentration effects along (a) the broken fiber $n = 0$ and (b) the nearest intact fiber $n = 1$ vs ξ for an elastic matrix ($\alpha = 0$), vs $\xi/\sqrt{t}$ for a Newtonian viscous matrix ($\alpha = 1$), and vs $\beta\xi/t^{\alpha/2}$ for a viscoelastic matrix ($\alpha < 1$).

$P_n^e(\xi) = L_n^{u,e}(\xi)+1$, (43), plotted vs ξ, the normalized (time-independent) fiber axial coordinate ($\beta = 1, \alpha = 0$). Thus, when $t = 1$, the fiber loads $P_n(\xi, t)$ for the viscous and viscoelastic cases agree closely with the elastic case. In real time, close agreement is seen when $\mathscr{T} = \mathscr{T}_c$, the characteristic time constant in (1) and (2).

Using Fig. 3(b) for the nearest intact fiber, $n = 1$, the effective overload length, $l_c(\mathscr{T})$, can be useful as a fiber length scale for the stress field produced by an isolated break. Specifically $l_c(\mathscr{T})$ is defined as the actual axial distance x from the peak stress at $\xi = 0$ to the point where the fiber load first recovers the remotely applied load p^*, i.e. $p(l_c(\mathscr{T}))/p^* \approx 1.00$ (defined before the "dip" and on one side of the break). As shown in Fig. 3(b), the normalized overload length in terms of the similarity variable z_c, is also close to 1.0 for both Cases I and II. Therefore in real dimensions, $l_c(\mathscr{T})$ scales with $(\mathscr{T}/\mathscr{T}_c)^{\alpha/2}$ or is proportional to the square root of $J(\mathscr{T})$, which is consistent with findings in Lifshitz and Rotem (1970), Gusev and Ovchinskii (1984), and Lagoudas *et al.* (1989).

For instance, using $z_c = 1.0$ and normalizations (4) and (26), we find that for the case $\alpha = 1$

$$l_c(\mathscr{T}) = \sqrt{\mathscr{T}}\sqrt{\frac{EA}{(\eta/w)h}}. \tag{76}$$

This result demonstrates that for a Newtonian viscous matrix, $l_c(\mathscr{T})$ increases in $\sqrt{\mathscr{T}}$ and inversely in $\sqrt{\eta/w}$. So for instance, two breaks i and j, one at x_i on fiber n and the other at x_j on fiber $n\pm 1$, will not strongly interact at times $\mathscr{T}$ satisfying $|x_i - x_j| > 2l_c(\mathscr{T})$. (In many publications, a 90% effective length is routinely defined, in which case, $z_c \approx 1.1$.)

When drawing upon an analogy with the time-independent case, time growing $l_c(\mathscr{T})$ may not be surprising. In both the elastic and linearly creeping matrix shear-lag models, when a fiber breaks, $P_0(\xi, t)$ almost exponentially builds up to the remotely applied load over a fiber length which scales with $\sqrt{E/G_e}$. Likewise, the surrounding intact fibers are overloaded over a complementary length, also scaling with $\sqrt{E/G_e}$. Therefore, one expects that time-dependent matrix relaxation $G(\mathscr{T})$ will cause the overload length to spread as $(\mathscr{T}/\mathscr{T}_c)^{\alpha/2}$ relative to the characteristic elastic load transfer length for a single fiber break. The opening displacement of a single break, $2U_0(0, t)$, scales in a similar fashion. Evaluating $V_n^u(\xi, t)$ in (28) or (47) at the break location (0, 0) yields $2V_n^u(0, t) = 2U_0(0, t) = (\pi t)^{1/2}$ for $\alpha = 1$ or $2U_0(0, t) = \pi t^{\alpha/2}/(2\beta)$ for $\alpha < 1$.

Figure 4 plots the normalized fiber tensile stress $P_n(\xi, t)$ on the subadjacent intact fibers, $n = 2$, 3, and 4, vs the normalized similarity variable $\xi/\sqrt{t}$ for the $\alpha = 1$ case (solid lines), and $P_n(\xi, t)$ vs $\beta\xi/t^{\alpha/2}$ for the viscoelastic case $0 < \alpha < 1$ (dashed lines), which is also also $P_n^e(\xi)$ vs ξ for the linear elastic case, $\alpha = 0$ ($\beta = 1$). Also evident from Fig. 5 is the decrease in peak stress concentrations, but increase in the overload lengths on fibers located further away from the break. For many polymeric materials, $\alpha \to 1$ as temperature increases, resulting in an increase in these overload lengths at longer times, though the profile shapes change little.

Note that in both Figs 3 and 4, along the plane of the break $\xi = 0$, the peak stress $P_n(0, t)$ for the various cases are all the same and time independent, i.e. $P_n(0, t) = L_n^{u,e}(0)+1$. From Hedgepeth (1961), we have

$$L_n^u(0, t) = L_n^{u,e}(0) = \frac{1}{4n^2 - 1}. \tag{77}$$

Remarkably the two sets of curves in Fig. 4 vary insignificantly and converge when n or $\xi \to \pm\infty$. The main differences are that the elastic and viscoelastic fiber stress concentrations decay faster along ξ from the break, and do not "dip" as far below unity as in the viscous case. Also for $|n| \geqslant 2$, the viscous solution is a little flatter near $\xi = 0$ and with a more extreme "dip". Had we plotted the exact solution based on (36) rather than (46) the curves would lie between the narrow extremes on Figs 3 and 4. The two term expansion (50) should also lie in-between provided α is not too large.

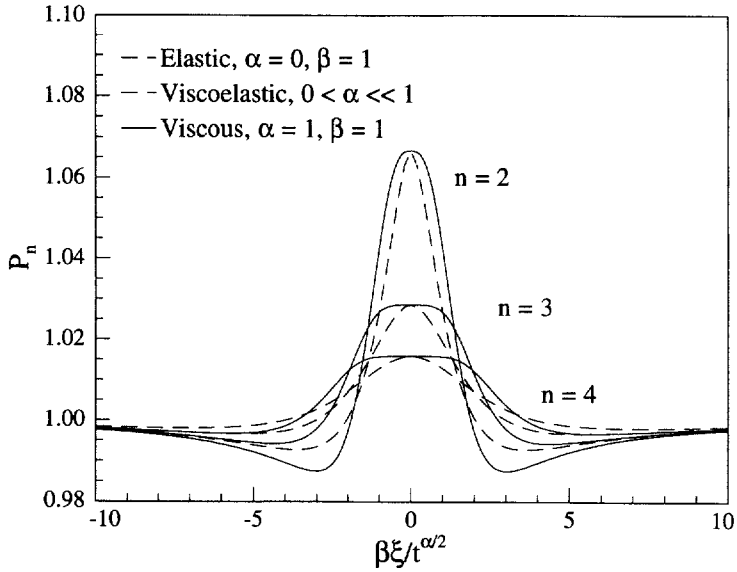

Fig. 4. Normalized fiber tensile load profiles showing stress concentration effects along the adjacent intact fibers $n = 2$, 3, and 4 vs ξ for an elastic matrix ($\alpha = 0$), vs $\xi/\sqrt{t}$ for a Newtonian viscous matrix ($\alpha = 1$), and vs $\beta\xi/t^{\alpha/2}$ for a viscoelastic matrix ($\alpha < 1$).

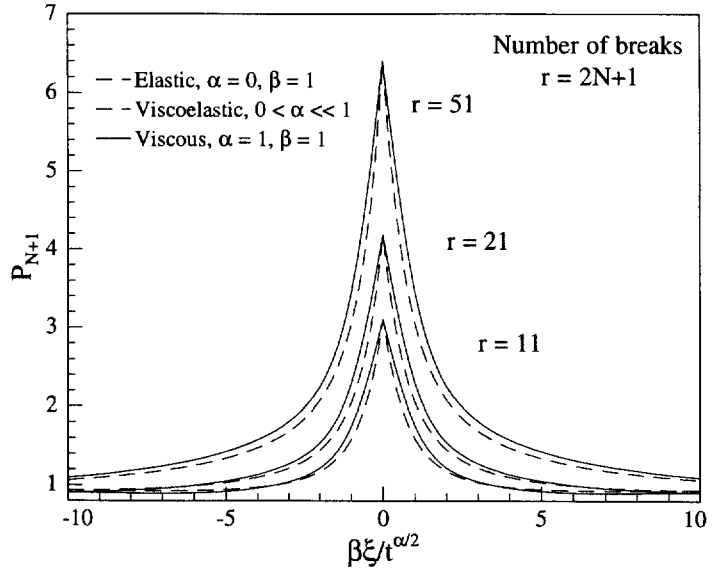

Fig. 5. Normalized fiber tensile load profiles on fiber $n = N+1$, which is the first intact fiber ahead of $r = 2N+1$ fiber breaks.

5.2. *Large transverse crack*

The VBI method was used to efficiently calculate the stress states around large transverse cracks (up to 51 breaks), and fully bridged cracks. In both examples, the breaks are aligned, and in this special case, $\{\mathbf{K}(t)\}$ is time-independent and thus, Methods I and III yield the same result. This special reduction also allows us to make direct correspondence with the elastic solution along the plane of the straight crack.

Figure 5 plots the normalized stress profiles on the first intact fiber ahead of a row of $r = 2N+1$ breaks, $P_{N+1}(\xi, t)$, vs the similarity variable $z = \xi/\sqrt{t}$, for Case I ($\alpha = 1$) and vs $z = \beta\xi/t^{\alpha/2}$ for Case II ($\alpha < 1$). As for a single break, $z_{c,r}$ is the value of z where $P_{N+1}(\xi, t) = 1.0$. Results in Fig. 5 show $z_{c,r}$ increases with r, and the overload region grows proportional to $z_{c,r}t^{\alpha/2}$ and hence at a rate increasing with r. Likewise in the crack opening

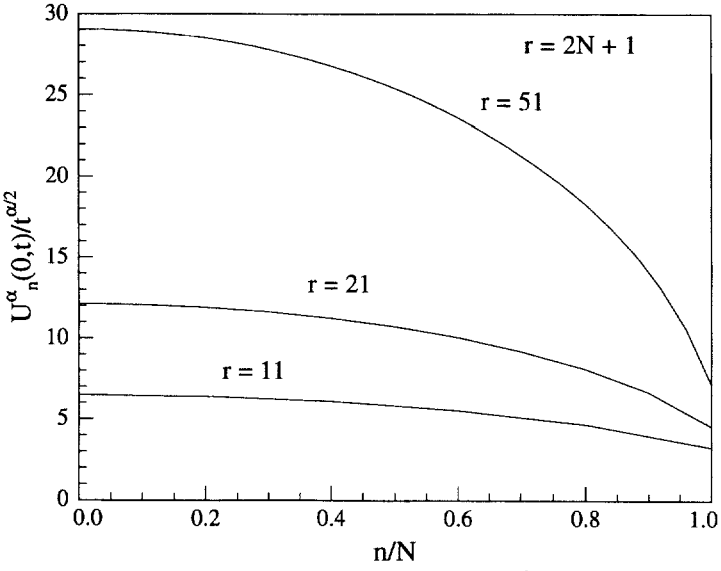

Fig. 6. The time-scaled half crack opening displacement $U_n^\alpha(0,t)/t^{\alpha/2}$ (see text) on one side of an r-sized crack vs n/N, wherein fibers $-N \leqslant n \leqslant N$ are broken.

displacements, $U_n(0,t)$, similarities in the basic forms between $V_n^u(0,t)$ for Cases I (28) and II (47) and $V_n^{u,e}(0)$ (44) suggest that for a crack, $U_n(0,t)/t^{1/2} = 2U_n^e(0)/\sqrt{\pi}$ for Case I and $U_n(0,t)/t^{\alpha/2} \approx U_n^e(0)/\beta$ for Case II. Figure 6 plots $U_n^\alpha(0,t)/t^{\alpha/2} = 2U_n^e(0)/\sqrt{\pi}$ for $\alpha = 1$ (Case I) and $U_n^\alpha(0,t)/t^{\alpha/2} = U_n^e(0)/\beta$ for $\alpha < 1$ (Case II), within a central crack containing $r = 2N+1$ breaks vs n/N, where $-N \leqslant n \leqslant N$. The results demonstrate that the crack opening displacements grow proportional to $t^{\alpha/2}$ for $\alpha \leqslant 1$, while taking nearly an elliptical shape vs n/N.

Both the effective load transfer lengths and opening displacements produced by an r-sized crack grow in time; however, the peak stresses along $\xi = 0$ ahead of the crack remain time-independent. As in the single break example, these crack plane stresses predicted by VBI and by the elastic shear-lag model are equivalent for the same r. For the elastic matrix case, Beyerlein *et al.* (1996) showed that this peak stress on the first intact fiber K_r is well approximated by

$$K_r \approx \frac{\sqrt{\pi}}{2}\sqrt{r+1}, \tag{78}$$

even for small r. For the sth intact fiber ahead of the last break

$$K_{r,s} \approx \frac{\sqrt{r+1}}{2\sqrt{s-1}} = \frac{K_r}{\sqrt{\pi(s-1)}}, \tag{79}$$

reminiscent of linear elastic fracture mechanics behavior.

We also perform the VBI analysis for a fully bridged crack, modeled as a row of alternating broken and intact fibers, wherein the breaks are aligned along the same transverse plane. The matrix acts as a creeping interface of thickness w, which allows the crack faces to slip relative to the intact, bridging fibers. For illustration, the crack spans a total of r^* fibers, and we consider the case where the fiber bridging fraction is 50%, that is, where alternate fibers are broken at $\xi = 0$. Our results show that the broken fiber ends separate proportional to $t^{\alpha/2}$, the overload lengths in the intact bridging fibers grow proportional to $t^{\alpha/2}$, and the peak stresses in the intact bridging fibers at $\xi = 0$ remain constant. As one may expect, the bridging fibers substantially reduce the rates of these processes and also the magnitude and sensitivity of the peak stress to r^*. For instance we calculate that for $r^* = 3$,

$K_{r^*} = 1.4084$, and $r^* = 201$, $K_{r^*} = 1.4489$. For the same 50% fully bridged crack but of infinite extent ($r^* = \infty$), the peak stress in the bridging fibers and opening displacements at the breaks, $2U_n(0, t)$, are all equal and can be calculated in closed form. As shown in Appendix C, in this limit ($r^* = \infty$) the peak stress in all bridging fibers is two, and $2U_n(0, t)$ for each break equals $4(t/\pi)^{1/2}$ for $\alpha = 1$ and $2t^{\alpha/2}/\beta$ for $\alpha < 1$.

5.3. *Weighting functions for multiple, staggered breaks*

Consider three staggered fiber breaks in adjacent fibers, as depicted in Fig. 7 and numbered $i = 1$, 2, and 3. In this case, $|\xi_1 - \xi_2| = |\xi_2 - \xi_3| = 2L$. When breaks are non-aligned, the corresponding $\{\mathbf{K}(t)\}$ changes in time. Growth in $\mathscr{K}_i(t)$ is associated with growth in the strength of interaction between break i and all others and takes a minimum value of 1.0 for an isolated break. For this and similar symmetric, staggered configurations, we find that changes in the $\mathscr{K}_j(t)$'s scale approximately with $t^{\alpha/2}/(\beta L)$, where $2L$ is the normalized distance between two adjacent breaks. This scaling implies that large separations between breaks lead to a slower rise in the level of interactions and hence stress concentrations with time.

In these cases, we can determine the limiting magnitudes of $\{\mathbf{K}(t)\}$ at $t = 0^+$ and $t = \infty$. At $t = 0^+$, only breaks one and three are interacting since they are aligned, i.e. $|\xi_1 - \xi_3| = 0$. As a result, $\{\mathbf{K}(0^+)\} = \{\mathscr{K}_1(0^+), \mathscr{K}_2(0^+), \mathscr{K}_3(0^+)\}^T = \{1.07, 1, 1.07\}^T$, by all three methods. In fact, these values are the same as those in the elastic problem. However in time, the fiber break ends separate and their effective load transfer lengths $l_c(\mathscr{T})$ interact, thereby increasing $\mathscr{K}_j$. Since break two is sandwiched between breaks one and three, $\mathscr{K}_2$ grows larger than $\mathscr{K}_1 = \mathscr{K}_3$. Apart from a brief initial drop caused by the "dips" in Figs 3(b) and 4, the $\mathscr{K}_j(t)$'s are nondecreasing, slowly approaching a limit as $t \to \infty$. Then, $(z_i - z_j) = (\xi_i - \xi_j)/t^{\alpha/2} \to 0$ and $\Lambda_{ij}(\infty) \to \mathscr{L}_n(0)$ of (77); that is, $\Lambda_{ij}(t)$ and $\mathscr{K}_j(t)$ approach values as though these breaks were aligned, i.e. $|\xi_i - \xi_j| = 0$. In this limit, $\Lambda_{12}(\infty) = \Lambda_{23}(\infty) = 1/3$ and $\Lambda_{13}(\infty) = 1/15$ using (77), and $\mathscr{K}_1(\infty) = \mathscr{K}_3(\infty) = 1.875$ and $\mathscr{K}_2(\infty) = 2.25$, by any method.

For $\alpha = 1$, differences between the $\mathscr{K}_j(t)$'s from Methods I and III are noticeable only for short times, with Method III tending to provide a slight overestimate. Clearly since $\alpha = 1$ exceeds the α range in which the approximate Laplace inversion method is valid, we do expect minor errors in employing Method II for $\alpha = 1$; however, for $\alpha < 1$, the differences in the predictions of Methods I and II are negligible.

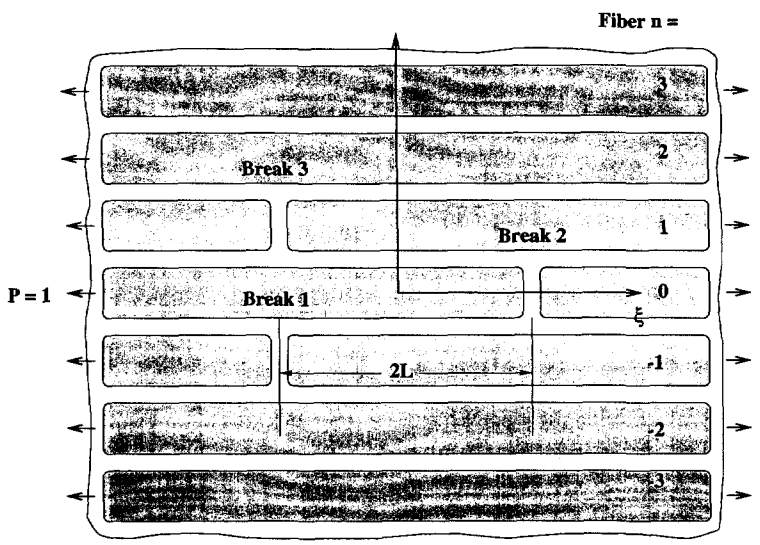

Fig. 7. Three staggered breaks in composite lamina space $2L$ apart in normalized coordinates. (Also used as a cell in a periodic microstructure.)

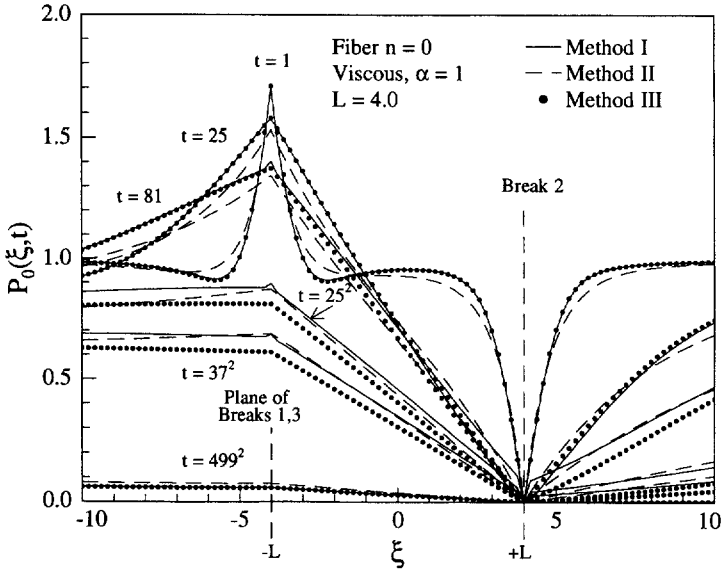

Fig. 8. Evolution of normalized fiber load profiles in time along fiber $n = 0$ in the three break configuration shown in Fig. 7 for the Newtonian viscous case $\alpha = 1$ as predicted from Methods I, II, and III.

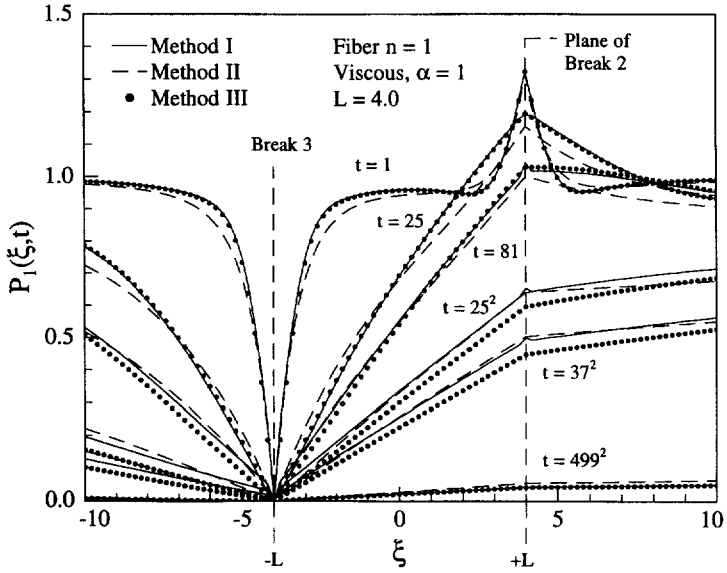

Fig. 9. Evolution of normalized fiber load profiles in time along fiber $n = 1$ in the three break configuration shown in Fig. 7 for the Newtonian viscous case $\alpha = 1$ as predicted from Methods I, II, and III.

5.4. *Stresses around multiple, staggered breaks*

In Figs 8–11, we show the normalized fiber tensile stress $P_n(\xi, t)$ profiles on the broken fibers $n = 0$ and 1 and on the adjacent fibers $n = 2$ and 3, respectively, for the Newtonian viscous case, $\alpha = 1$ at various times using Methods I, II, and III. By symmetry, $P_n(\xi, t)$ for fibers $n = 1$, 2 and 3 are the same as those in fibers $n = -1$, -2, and -3, respectively. As indicated, the overlap length between these breaks, $L = 4$, is selected such that the breaks are essentially non-interacting at $t = 1$.

For the broken fibers, the overloads decay as does the rate at which the tensile stresses build up from the break. At the same time, the load transferred from these broken fibers to the adjacent unbroken fibers $n = 2$ and 3 gradually increases with time. For instance,

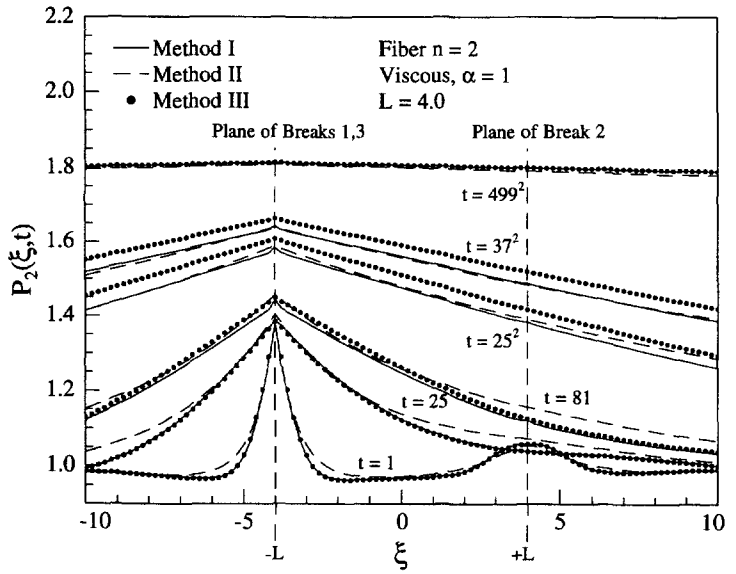

Fig. 10. Evolution of normalized fiber load profiles in time along fiber $n = 2$ in the three break configuration shown in Fig. 7 for the Newtonian viscous case $\alpha = 1$ as predicted from Methods I, II, and III.

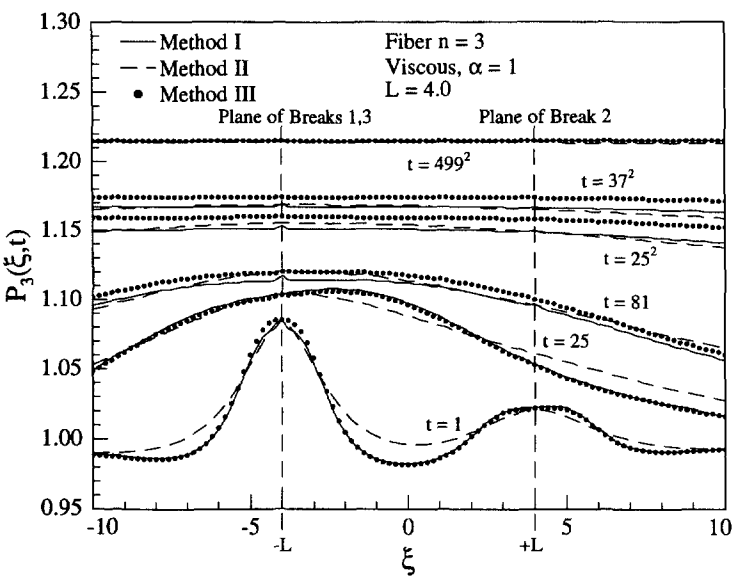

Fig. 11. Evolution of normalized fiber load profiles in time along fiber $n = 3$ in the three break configuration shown in Fig. 7 for the Newtonian viscous case $\alpha = 1$ as predicted from Methods I, II, and III.

for fiber $n = 2$, the maximum tensile stress increases from 1.33 at $t = 1$–1.8 at $t = 499^2$, and will eventually approach a maximum of 1.83, the elastic prediction for three aligned breaks. However, the stress distributions elsewhere become more dispersed compared to those predicted by the elastic solution. Also note in Figs 8–11, that the location of the maximum stress along any fiber remains the same. Locations and time increasing magnitudes and spreading of the peak stresses would have important effects in predicting fiber failure progression as new flaws are encountered in fibers.

To minimize errors in Method I, time increments used in evaluating $L_n(\xi, t)$ (65) by numerical integration were orders of magnitude smaller than the change in stress state. In this example (Fig. 7), the differences between the stress profiles of Method I and the

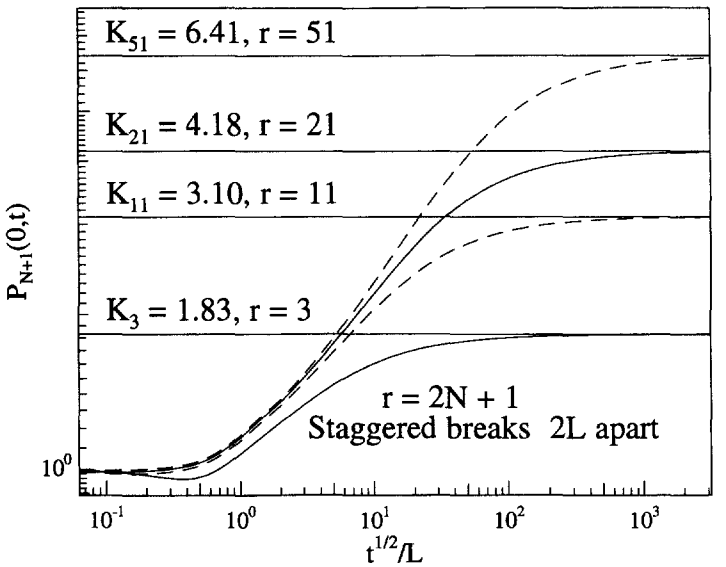

Fig. 12. Evolution of the stress concentration at $\xi = 0$ in the first intact fiber, $P_{N+1}(0, t)$ ahead of an r staggered fiber breaks.

approximate Method II become small for long times (e.g. in Figs 8–11 for $t > 25$). On the other hand, the other approximate approach Method III yields nearly the same stress predictions as Method I at short times, e.g. $t \leqslant 25$, and at long times (e.g. $t = 499^2$). For the broken fibers $n = 0$ and 1, Method III predicts a faster decay in tensile stress away from break sites at intermediate times. According to the methodology of Method III, this trend is a result of calculating $P_n(\xi, t)$ by simply using the influence and weighting functions at the current time, thus, assuming these conditions operated since application of the load at $t = 0$. However for the nearest intact fibers $n = 2$, 3, these differences have a negligible effect on stress concentrations; only at long times does Method III yield slightly higher (conservative) tensile loads. When applying Method III to Case II, the resulting tensile stresses are only slightly higher than those of Methods I and II and scale as $t^{\alpha/2}/(\beta L)$.

We extend this staggered break pattern from three breaks to $r = 2N+1 = 11$, 21, and 51 breaks. That is, all fibers within $-N \leqslant n \leqslant N$ contain one break at locations alternating between $\xi = -L$ and L, thus, forming a damage zone with overlapping fiber ends. For each damage zone of length r, we show in Fig. 12 the evolution of the normalized fiber tensile stress on the first intact fiber $P_{N+1}(0, t)$ at $\xi = 0$ for $\alpha = 1$ vs $t^{1/2}/L$. Initially the stress fields of the breaks are non-interacting at $\xi = 0$, and so $P_{N+1}(0, t) \approx 1$. (The initial dip in the $r = 3$ curve is related to the dip in Fig. 3.) However, in time, $P_{N+1}(0, t)$ increases as if an r-sized crack had formed. The limit K_r, indicated on Fig. 12, is calculated exactly and is well-predicted by (78).

Recall that when $t = 1$ or $\mathscr{T} = \mathscr{T}_c$, the elastic Hedgepeth shear-lag result closely matches the linear viscous result. Thus, one can use Fig. 12 to determine the corresponding linear elastic value for the crack-tip stress concentration. For instance, if $L = 10$, or in terms of "real" distance, $l = 10(wEAJ_e/h)^{1/2}$ (widely space breaks), the stress predicted by the elastic solution would correspond to the value of $P_{N+1}(0, t)$ at $t^{1/2}/L = 1/10$ in Fig. 12, which is unity for all r. However, if $L = 10^{-2}$ (closely spaced breaks), then the elastic prediction corresponds to the stress concentrations where the $P_{N+1}(0, t)$ curves intersect $t^{1/2}/L = 10^2$.

For 51 staggered breaks, Fig. 13 shows the time evolution of the normalized relative opening displacement $[U_0(L, t) - L]/L$ (or $V_0(L, t)/L$) of the center break at $n = 0$ and at $\xi = L$ for $\alpha = 1$. Here $U_0(L, t)$ corresponds to the displacement of the fractured end within the overlap zone $|\xi| \leqslant 2L$. For comparison we also plot the creep response of a 51 fiber break crack, which we know from Fig. 6, increases proportional to $t^{1/2}$. During a short transient period (1st stage), the stress fields of the breaks aligned at $\xi = L$ do not interact

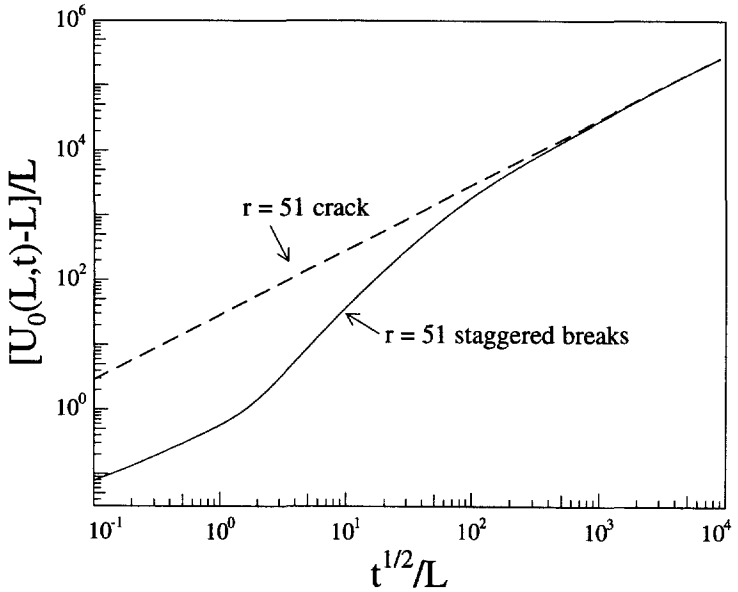

Fig. 13. Evolution of the relative opening displacement $U_0(L, t) - L$ of the center break within an $r = 51$ staggered break damage zone.

with those aligned at $\xi = -L$, and as a result $U_0(L, t) \propto t^{1/2}$, as shown in Fig. 13. Once these breaks interact, $U_0(L, t)$ increases proportional to t, or at a steady rate, during the intermediate times (2nd steady-state stage) in Fig. 13. In the long time limit (3rd stage), $U_0(L, t)$ gradually approaches the creep response of a transverse crack consisting of 51 fiber breaks, and therefore once again increases proportional to $t^{1/2}$.

5.5. *Stresses around multiple breaks in a periodic microstructure*

We also studied laminae with periodic arrays of breaks. The unit cell consisted of the seven fibers with breaks shown in Fig. 7. The tensile stresses in the broken fibers decayed at a much faster rate than those in Figs 9 and 10, and the tensile stress concentrations in the intact fibers increased at a much faster rate and achieved a more uniform distribution than those in the previous non-periodic case. The rapid reduction in shear stress transfer along ξ as $t \to \infty$, caused the broken fibers to completely unload along their lengths, and the intact fibers ultimately to sustain all the applied tensile stress equally. Thus, in the long time limit, the composite was found to behave as an equal load-sharing fiber bundle, where each survivor sustained a stress concentration of $1/(1-\chi)$, where χ is the fraction of fibers containing breaks (e.g. $\chi = 3/7$ in Fig. 7). So despite all the approximations and local nature of the influence functions, the correct limit was achieved.

6. DISCUSSION AND FUTURE WORK

We have developed an efficient computational mechanics technique, called viscous break interaction (VBI), which determines as a function of time, the stress and displacement distributions around an arbitrary array of fiber breaks in a planar unidirectional fiber composite. The present version assumes that fibers are linearly elastic and the matrix creeps in shear according to a linear viscous or viscoelastic power-law in time. While the initial elastic behaviour of the matrix has not been modeled directly, we have shown that it can be approximated quite well.

For transversely aligned breaks, such as a crack, the problem is greatly simplified in that the weighting functions $\mathscr{K}_1(t)$, $\mathscr{K}_2(t)$, ... (strength of each break interaction) are actually constant in time. This means that the peak tensile loads in neighboring intact fibers remain fixed (though the overload transfer length along these fibers spread as $t^{\alpha/2}$, increasing the likelihood of further breaks). Also the fracture ends in the crack separate as $t^{\alpha/2}$. This

creep crack opening response is accommodated by the reduction in the composite stiffness (or matrix creep) and not by crack growth, fiber-matrix debonding, or fiber degradation. Restricting the model to steady interactions between fiber breaks (i.e. constant $\mathscr{K}_i(t)$'s) corresponds to the primary creep stage in a composite.

On the other hand, once the stress fields of the fiber breaks begin to influence one another, the $\mathscr{K}_i(t)$'s increase in time, forcing the peak fiber loads typically to increase in time and the opening displacements to deviate from the $t^{\alpha/2}$ scaling. In fact, for certain staggered fiber break patterns with overlapping fiber segments, the opening displacements will grow as t^{α}, which for $\alpha = 1$ is linear in time. This feature will lead to a secondary creep stage. Also we have shown that even for simple non-aligned break patterns, the evolving stress and displacement profiles are quite complex. One can readily appreciate that increasing fiber loads will lead to further breaks, and the potential for an accelerated tertiary creep stage, as well as localization leading rapidly to failure. This feature of time growing fiber break interactions differentiates the current VBI model from previous models.

Future applications will be directed towards simulating creep fracture in large, finite-sized composites and large composites with periodic microstructures (discontinuous fiber composite). The former case will be relevant to investigations into the composite size effect and the latter to investigations into the effects of local geometry, such as variations in fiber aspects ratios and spatial distances between breaks, on the primary, secondary, and tertiary stages of composite creep strain. Previous investigations assuming Weibull fiber strength have illustrated the effects of variability on static fracture resistance and sensitivity to a pre-existing notch, and have aided in developing probability models for composite strength (Beyerlein and Phoenix, 1997a,b). Future work will also assume statistical variation in fiber strength or in cavitation threshold strength, and the VBI technique will be used to generate sequential, random creep-driven fiber breaks in a Monte-Carlo framework. The goal will be to develop models that better interpret long term test data and serve as a design tool in optimizing lifetime while reducing component variability.

Acknowledgements—This material is based upon work supported under a National Science Foundation Graduate Research Fellowship. I.J.B. also acknowledges support under an NSF/GEE fellowship (Grant no. EID-91-16878). The authors would also like to acknowledge support from the AFOSR University Research Initiative (Grant no. F49620-93-1-0235) and from the National Science Foundation (Grant no. DMR-9505859). The authors are grateful to Professor C. Y. Hui for his help in deriving the inverse Laplace transforms.

REFERENCES

Abramowitz, M. and Stegun, I. A., eds (1970) *Handbook of Mathematical Functions*. Dover Publications, New York.

Batchelor, G. K. (1971) The stress generated in a non-dilute suspension of elongated particles by pure straining motion. *Journal of Fluid Mechanics* **46,** 813–820.

Beyerlein, I. J. and Phoenix, S. L. (1996) Stress concentrations around multiple fiber breaks in an elastic matrix with local yielding or debonding using quadratic influence superposition. *Journal of the Mechanics and Physics of Solids* **44,** 1997–2039.

Beyerlein, I. J., Phoenix, S. L. and Sastry, A. M. (1996) Comparison of shear-lag theory and continuum fracture mechanics for modeling fiber and matrix stresses in an elastic cracked composite lamina. *International Journal of Solids and Structures* **33,** 2543–2574.

Beyerlein, I. J. and Phoenix, S. L. (1997a) Statistics of fracture for an elastic notched composite lamina containing Weibull fibers—Part I: features from monte-carlo simulation. *Engng. Fract. Mech.* **57,** 241–265.

Beyerlein, I. J. and Phoenix, S. L. (1997b) Statistics of fracture for an elastic notched composite lamina containing Weibull fibers—Part II: probability models for crack growth. *Engng. Fract. Mech.* **57,** 267–299.

Beyerlein, I. J. and Phoenix, S. L. (1997c) Stress profiles and energy release rates around fiber breaks in a lamina with propagating zones of matrix yielding and debonding. *Comp. Sci. Technol.* **57,** 869–885.

Beyerlein, I. J., Amer, M. S., Schadler, L. S. and Phoenix, S. L. (1998) New methodology for determining *in situ* fiber, matrix, and interface stresses in damaged multifiber composites. *Sci. Engng. Comp. Mat.*, submitted.

Christensen, R. M. (1982) *Theory of Viscoelasticity*. Academic Press, New York.

Dragone, T. L. and Nix, W. D. (1990) Geometric factors affecting the internal stress distribution and high temperature creep rate of discontinuous fiber reinforced metals. *Acta Metall. Mater.* **38,** 1941–1953.

Du, Z. Z. and McMeeking, R. M. (1995) Creep models for metal matrix composites with long brittle fibers. *Journal of the Mechanics and Physics of Solids* **43,** 701–726.

Evans, A. G. and Rana, A. (1980) High temperature failure mechanisms in ceramics. *Acta Metall.* **28,** 129–141.

Goddard, J. D. (1976) The stress field of slender particles oriented by a non-Newtonian extensional flow. *Journal of Fluid Mechanics* **78,** 177–206.

Gusev, Y. S. and Ovchinskii, A. S. (1984) Computer modeling of failure processes of fiber-reinforced composite materials under the effect of a constantly acting tensile load. *Mech. Comp. Mater.*, March–April, No. 2, 196–203.

Haddad, Y. M. and Iyer, S. S. (1996) On the characterization of the stress-relaxation response of a class of linear viscoelastic material using acousto-ultrasonics: a pattern recognition approach. *Mech. Mater.* **24,** 199–211.

Harlen, O. G. and Koch, D. L. (1992) Extensional flow of a suspension of fibers in a dilute polymer solution. *Physics of Fluids A* **4,** 1070–1073.

Hedgepeth, J. M. (1961) Stress concentrations in filamentary structures. NASA TN D-882.

He, J., Beyerlein, I. J. and Clarke, D. R. (1998) Load transfer from broken fibers in continuous fiber Al_2O_3–Al composite and dependence on local volume fraction. *Journal of the Mechanics and Physics of Solids*, to appear.

Hunter, R. J. (1987) *Foundations of Colloid Science* **1,** 76–89. Clarendon Press, Oxford.

Ibnabdeljalil, M. and Curtin, W. A. (1996) Strength and reliability of fiber-reinforced composites: local load-sharing and associated size effects. *International Journal of Solids and Structures* **34,** 2649–2668.

Ibnabdeljalil, M. and Phoenix, S. L. (1995) Creep rupture of brittle matrix composites reinforced with time dependent fibers: scalings and Monte Carlo simulations. *Journal of the Mechanics and Physics of Solids* **43,** 897–931.

Iyengar, N. and Curtin, W. A. (1997) Time-dependent failure in fiber-reinforced composites by shear creep at the fiber-matrix interface. *Acta Mater.* **45,** 3419–3429.

Kibler, K. G. and Carter, H. G. (1979) Viscoelastic parameters of epoxy resin from thermomechanical and electric conductivity measurements. In *Composite Materials: Testing and Design*, ed. S. W. Tsai, ASTM STP 674, pp. 282–288.

Lagoudas, D. C., Hui, C. Y. and Phoenix, S. L. (1989) Time evolution of overstress profiles near broken fibers in a composite with a viscoelastic matrix. *International Journal of Solids and Structures* **25,** 45–66.

Lee, S., Yeng, S. M. and Yang, J. M. (1996) Modeling and simulation of the effect of fiber breakage in creep behavior of fiber reinforced metal matrix composites. *Mech. Mater.* **21,** 303–312.

Lifshitz, J. M. and Rotem, A. (1970) Time-dependent longitudinal strength of unidirectional fibrous composites. *Fibre Sci. Technol.* **3,** 1–20.

Lilholt, H. (1985) Creep of fibrous composite materials. *Comp. Sci. T.* **22,** 277–294.

Mason, D. D., Hui, C. Y. and Phoenix, S. L. (1992) Stress profiles around a fiber break in a composite with a nonlinear, power law creeping matrix. *International Journal of Solids and Structures* **23,** 2829–2854.

Menon, M. N., Fang, H. T., Wu, D. C., Jenkins, M. G. and Ferber, M. K. (1994) Creep and stress rupture behavior of an advanced silicon nitride: Parts I–III. *J. Am. Ceram. Soc.* **77,** 1217–1241.

Onck, P. and Van Der Giessen, E. (1997) Influence of microstructural variations on steady-state creep and facet stresses in 2-D freely sliding polycrystals. *International Journal of Solids and Structures* **34,** 703–726.

Otani, H., Phoenix, S. L. and Petrina, P. (1991) Matrix effects on lifetime statistics for carbon fibre–epoxy microcomposites in creep rupture. *J. Mater. Sci.* **26,** 1955–1970.

Phoenix, S. L., Schwartz, P. and Robinson IV, H. H. (1988) Statistics for the strength and lifetime in creep-rupture of model carbon/epoxy composites. *Comp. Sci. Technol.* **32,** 81–120.

Pipes, R. B., Hearle, J. W. S., Beaussart, A. J. and Okine, R. K. (1991) Influence of fiber length on the viscous flow of an oriented fiber assembly. *J. Comp. Mater.* **25,** 1379–1390.

Pipes, R. B. (1992) Anisotropic viscosities of an oriented fiber composite with a power-law matrix. *J. Comp. Mater.* **26,** 1536–1552.

Rabotnov, Y. N. (1969) The fundamental experimental facts and phenomenological theories. In *Creep Problems in Structural Members*, Vol. 7, pp. 172–264. North-Holland Publishing Company, London.

Raghavan, J. and Meshii, M. (1996) Time-dependent damage in carbon fibre-reinforced polymer composites. *Composites* **27A,** 1223–1227.

Sastry, A. M. and Phoenix, S. L. (1993) Load redistribution near non-aligned fibre breaks in a two-dimensional unidirectional composite using break-influence superposition. *J. Mater. Sci. Lett.* **12,** 1596–1599.

Schapery, R. A. (1967) Stress analysis of viscoelastic composite materials. *J. Comp. Mater.* **1,** 228–267.

Song, Y., Bao, G. and Hui, C. Y. (1995) On creep of unidirectional fiber composites with fiber damage. *Acta Metall. Mater.* **43,** 2615–2623.

Stumpf, H. and Schwartz, P. (1993) A Monte Carlo simulation of the stress rupture of seven-fiber microcomposites. *Comp. Sci. Technol.* **49,** 251–263.

Tsai, R. L. and Raj, R. (1982) Overview 18: Creep fracture in ceramics containing small amounts of a liquid phase. *Acta Metall.* **30,** 1043–1058.

Zhou, S. J. and Curtin, W. A. (1995) Failure of fiber composite: a lattice Green function model. *Acta Metall. Mater.* **43,** 3093–3104.

APPENDIX A

In the case $\alpha = 1$, $s\underline{\mathscr{G}}_0(s)$ from (17) and (18) is simply s, and (20) reduces to

$$V_n^u(\xi, t) = \operatorname{sgn}(\xi)\frac{1}{4}\int_0^{\pi} \cos(n\theta)\mathbf{L}^{-1}[s^{-3/2}\exp\{-2|\xi|\sin(\theta/2)\sqrt{s}\}]\,d\theta. \tag{A1}$$

The inverse Laplace transform in the integrand of (A1), can be found in most mathematical tables (e.g. Abramowitz and Stegun, 1970) from the pair

$$\underline{f}(s) = s^{-3/2}\exp(-\hat{a}|\xi|\sqrt{s}), \quad k \geqslant 0 \tag{A2}$$

and

$$\mathscr{L}^{-1}(\underline{f}(s)) = f(t) = 2\sqrt{\frac{t}{\pi}}\exp\left(-\frac{(\hat{a}|\xi|)^2}{4t}\right) - \hat{a}|\xi|\,\mathrm{erfc}\left(\frac{\hat{a}|\xi|}{2\sqrt{t}}\right) \tag{A3}$$

where in general,

$$\hat{a} = 2\sin(\theta/2)/\sqrt{\Gamma(\alpha+1)}, \tag{A4}$$

which evaluates to $\hat{a} = 2\sin(\theta/2)$ for the present case $\alpha = 1$. Also erfc(·) is the complement of the error function, i.e. $\mathrm{erfc}(x) = 1 - \mathrm{erf}(x)$. Substituting the inverse Laplace transform into (A1) and making the key transformation, $z = \xi/\sqrt{t}$, we obtain the result (28) for $V_n^u(\xi, t)$. We may use the same procedure to obtain $L_n^u(\xi, t)$, given in (31), or simply use $L_n^u(\xi, t) = \partial V_n^u(\xi, t)/\partial\xi$.

An alternative method to obtain $L_n^u(\xi, t) = \mathscr{L}_n(z)$ involves applying the discrete Fourier transform pair,

$$\underline{\mathscr{L}}(z, \theta) = \sum_{n=-\infty}^{\infty} \mathscr{L}_n(z)\exp(-in\theta) \tag{A5}$$

and

$$\mathscr{L}_n(z) = \frac{1}{2\pi}\int_{-\pi}^{\pi} \underline{\mathscr{L}}(z, \theta)\exp(in\theta)\,\mathrm{d}\theta, \tag{A6}$$

to the equilibrium equation (33). This yields,

$$\frac{\mathrm{d}^2\underline{\mathscr{L}}(z, \theta)}{\mathrm{d}z^2} + 2\sin^2(\theta/2)z\frac{\mathrm{d}\underline{\mathscr{L}}(z, \theta)}{\mathrm{d}z} = 0. \tag{A7}$$

Solving (A7) and applying the transformed boundary conditions, $\underline{\mathscr{L}}(\pm\infty, \theta) = 0$, for all n and $t \geqslant 0$, and $\underline{\mathscr{L}}(0, \theta) = -(2/\pi)\sin(\theta/2)$ at $n = 0$, $z = 0$, we get

$$\underline{\mathscr{L}}(z, \theta) = -\frac{2}{\pi}\sin(\theta/2)\,\mathrm{erfc}(\sin(\theta/2)z). \tag{A8}$$

Inverting (A8) using (A6) to regain dependence on n, we again obtain (31) for $L_n^u(\xi, t)$.

APPENDIX B

Here we consider the case $0 < \alpha < 1$ and derive closed-form expression for the inverse Laplace transform functions found in $L_n^u(\xi, t)$, $V_n^u(\xi, t)$ and $T_n^u(\xi, t)$ of (20)–(23). The inversion of the Laplace transforms were obtained by contour integration. The selection closed contour travels up the imaginary axis positioned at a sufficiently large positive real value γ, along the top and bottom branches of the negative real axis, around a small ε-radius circle around zero, and along a counter-clockwise semicircle centered at γ. For all functions considered, an integral along the semicircle tends to zero as its radius $\to \infty$.

The solutions are in integral form, so we are motivated to give a series expansion of the results to compare with those obtained using the direct method of Schapery (1967) for approximate Laplace inversion, described in Section 3.4. We also take the limit $\alpha \to 0$ to show that the original results of Hedgepeth (1961) are recovered.

To simplify the notation, the following analyses consider only the right half plane, $\xi \geqslant 0$. (Recall that $L_n^u(\xi, t)$ is symmetric, and $V_n^u(\xi, t)$ and $T_n^u(\xi, t)$ are anti-symmetric in ξ.)

B.1. Fiber loads

Substituting the matrix constitutive law (18) for $s\underline{\mathscr{G}}(s)$ into $L_n^u(\xi, t)$ (21) yields the desired quantity to invert

$$f(\xi, t) = \mathbf{L}^{-1}\left[\frac{1}{s}\exp(-\hat{a}\xi s^{\alpha/2})\right] \tag{B1}$$

where $\hat{a}$ is given in (A4). Applying the usual Laplace inversion integral formula (Bromwich) and evaluating this through contour integration as described above, yields

$$f(\xi, t) = 1 - \frac{1}{\pi}\int_0^{\infty}\frac{\exp(-rt)}{r}[\exp\{-\hat{a}\xi\cos(\pi\alpha/2)r^{\alpha/2}\}] \times \sin\{\hat{a}\xi\sin(\pi\alpha/2)r^{\alpha/2}\}\,\mathrm{d}r. \tag{B2}$$

In this case, the integral around the small ε-circle tends to 1 as $\varepsilon \to 0$.

Applying the variable transformations, $u = r^{\alpha/2}$, $v = u\xi/z$, where $z = \xi/t^{\alpha/2}$, and using the fact that $f(\xi, t) = 0$ for $\xi > 0$, $f(\xi, t)$ transforms to

$$f_0(z) = f(\xi, (|\xi|/z)^{2/\alpha})$$

$$= \frac{2}{\pi\alpha}\int_0^{\infty}[\exp\{-\hat{a}\cos(\pi\alpha/2)zv\}]$$

$$\times \sin\{\hat{a}\sin(\pi\alpha/2)zv\}\frac{1-\exp(-v^{2/\alpha})}{v}\mathrm{d}v. \tag{B3}$$

In order to evaluate the above expression, we first rewrite $1-\exp(-v^{2/\alpha})$ in (B3) as the sum of a unit step function at $v=\Gamma(1+\alpha/2)$ and a deviation function $\Delta_\alpha(v)$, which decays to zero as $\alpha\to 0$. That is

$$1-\exp(-v^{2/\alpha}) = \mathbf{H}(v-\Gamma(1+\alpha/2))+\Delta_\alpha(v) \tag{B4}$$

where $\mathbf{H}(\cdot)$ is the Heaviside step function, and thus $\Delta_\alpha(v)$ must be

$$\Delta_\alpha(v) = 1-\exp(-v^{2/\alpha}), \quad \text{for} \quad 0\leqslant v<\Gamma(1+\alpha/2), \tag{B5a}$$

$$\Delta_\alpha(v) = -\exp(-v^{2/\alpha}), \quad \text{for} \quad \Gamma(1+\alpha/2)\leqslant v<\infty. \tag{B5b}$$

Inserting (B4) into (B3) enables us to break up $f_0(z)$ as

$$f_0(z) = f_1(z)+f_2(z) \tag{B6}$$

where

$$f_1(z) = \frac{2}{\pi\alpha}\int_{\Gamma(1+\alpha/2)}^{\infty}\frac{\exp\{-\hat{a}\cos(\pi\alpha/2)zv\}}{v}\sin\{\hat{a}\sin(\pi\alpha/2)zv\}\,\mathrm{d}v, \tag{B7}$$

and

$$f_2(z) = \frac{2}{\pi\alpha}\int_0^{\infty}\Delta_\alpha(v)\frac{\exp\{-\hat{a}\cos(\pi\alpha/2)zv\}}{v}\sin\{\hat{a}\sin(\pi\alpha/2)zv\}\,\mathrm{d}v. \tag{B8}$$

Referring to standard integral tables, $f_1(z)$ can be evaluated and is

$$f_1(z) = -\frac{2}{\pi\alpha}I\{E_1[\tilde{a}z\exp(i\pi\alpha/2)]\}, \tag{B9}$$

where

$$\tilde{a} = \hat{a}\Gamma(1+\alpha/2), \tag{B10}$$

and where $E_1(\phi)$ is the exponential integral with complex variable argument ϕ, and $I(\phi)$ means the imaginary part of ϕ. A series expansion for $f_1(v)$ can be found by substituting into (B9) the series expansion for $E_1(\phi)$, applicable to $|\arg(\phi)|<\pi/2$, which translates to $\alpha<1$ for our case (Abramowitz and Stegun, 1970) yielding,

$$f_1(z) = 1+\frac{2}{\pi\alpha}\sum_{n=1}^{\infty}\frac{(-1)^n(\tilde{a}z)^n\sin(n\pi\alpha/2)}{nn!}, \quad 0<\alpha<1. \tag{B11}$$

For the first- and second-order terms for $f_1(z)$ corresponding to small α, we apply the Taylor series expansion of $\sin(n\pi\alpha/2)/(n\pi\alpha/2)$ about $n\pi\alpha/2=0$ and find that,

$$f_1(z) \approx \exp\{-\tilde{a}z\}+\frac{(\pi\alpha/2)^2}{6}\exp\{-\tilde{a}z\}\tilde{a}z(1-\tilde{a}z). \tag{B12}$$

In evaluating $f_2(z)$ of (B8), we first expand the exponential function in a Taylor's series about $\hat{a}zv[\cos(\pi\alpha/2)-\Gamma(1+\alpha/2)]=0$ and the sine function about $\hat{a}\sin(\pi\alpha/2)zv=0$. We then integrate, making use of the following four facts,

$$\int_0^{\infty}\Delta_\alpha(v)\,\mathrm{d}v = 0 \tag{B13a}$$

$$\int_0^{\infty}\Delta_\alpha(v)v\,\mathrm{d}v = \frac{1}{2}(\Gamma(1+\alpha/2)^2-\Gamma(1+\alpha)) \tag{B13b}$$

$$\int_0^{\infty}\frac{\Delta_\alpha(v)}{v}\mathrm{d}v = \frac{1}{12}\left(\frac{\pi\alpha}{2}\right)^2 \tag{B13c}$$

$$\int_0^{\infty}\frac{\Delta_\alpha(v)}{v^2}\mathrm{d}v = \Gamma(1-\alpha/2)-\frac{1}{\Gamma(1+\alpha/2)} \tag{B13d}$$

where $\Delta_\alpha(v)$ is defined in (B4). Retaining the lowest order terms in z and in α, we approximate $f_2(z)$ as

$$f_2(z) \approx \frac{(\tilde{a}z)^2}{6}\left(\frac{\pi\alpha}{2}\right)^2 \exp\{-\tilde{a}z\}. \tag{B14}$$

B.2. Fiber displacements

Substituting the matrix constitutive law (17) for $s\underline{\mathscr{G}}(s)$ into $V_n^u(\xi, t)$ (20) yields for the quantity to be inverted

$$g(\xi, t)\sqrt{\Gamma(\alpha+1)} = \mathbf{L}^{-1}\left[\frac{1}{s^{1+\alpha/2}}\exp(-\hat{a}|\xi|s^{\alpha/2})\sqrt{\Gamma(\alpha+1)}\right]. \tag{B15}$$

Performing the Laplace inversion as described above yields

$$g(\xi, t) = \frac{1}{\pi}\int_0^\infty \frac{1-\exp(-rt)}{r^{\alpha/2+1}}[\exp\{-\hat{a}|\xi|\cos(\pi\alpha/2)r^{\alpha/2}\}] \times \sin\{\hat{a}|\xi|\sin(\pi\alpha/2)r^{\alpha/2}+\pi\alpha/2\}\,dr, \tag{B16}$$

where a useful step is to first find the inversion of the time derivative of (B15) and then to integrate with respect to time to obtain $g(\xi, t)$. Applying to $g(\xi, t)$, the same series of variable transformations used to transform (B2) into (B3), we get

$$\begin{aligned} g_0(z) &= t^{-\alpha/2}g(\xi,(|\xi|/z)^{2/\alpha}) \\ &= \frac{2}{\pi\alpha}\int_0^\infty [\exp\{-\hat{a}\cos(\pi\alpha/2)zv\}] \\ &\quad \times \sin\{\hat{a}\sin(\pi\alpha/2)zv+\pi\alpha/2\}\frac{1-\exp(-v^{2/\alpha})}{v^2}dv. \end{aligned} \tag{B17}$$

Substituting (B4) into (B17), we break up $g_0(v)$ as

$$g_0(z) = g_1(z)+g_2(z), \tag{B18}$$

where,

$$g_1(z) = \frac{2}{\pi\alpha}\int_{\Gamma(1+\alpha/2)}^\infty \frac{\exp\{-\hat{a}\cos(\pi\alpha/2)zv\}}{v^2} \times \sin\{\hat{a}\sin(\pi\alpha/2)zv+\pi\alpha/2\}\,dv, \tag{B19}$$

and

$$g_2(z) = \frac{2}{\pi\alpha}\int_0^\infty \Delta_\alpha(v)\frac{\exp\{-\hat{a}\cos(\pi\alpha/2)zv\}}{v^2} \times \sin\{\hat{a}\sin(\pi\alpha/2)zv+\pi\alpha/2\}\,dv. \tag{B20}$$

Applying the trigonometric identity, $\sin(a+b) = \sin(a)\cos(b)+\sin(b)\cos(a)$, to $g_1(v)$ and integrating the two resulting integrals by parts, we get

$$\begin{aligned} g_1(z) = \frac{2}{\pi\alpha\Gamma(1+\alpha/2)}&\exp\{-\tilde{a}\cos(\pi\alpha/2)z\}\sin\{\tilde{a}\sin(\pi\alpha/2)z+\pi\alpha/2\} \\ &- \frac{2\tilde{a}z}{\pi\alpha\Gamma(1+\alpha/2)}\int_1^\infty \frac{\exp\{-\tilde{a}\cos(\pi\alpha/2)zv\}}{v}\sin\{\tilde{a}\sin(\pi\alpha/2)zv\}\,dv. \end{aligned} \tag{B21}$$

Notice that the second integral in (B21) is $\tilde{a}zf(v)/\Gamma(1+\alpha/2)$; so substituting (B12) into (B21), $g_1(z)$ is approximately

$$\begin{aligned} g_1(z) \approx \frac{1}{\Gamma(1+\alpha/2)}\Big\{&\frac{2}{\pi\alpha}\exp\{-\tilde{a}\cos(\pi\alpha/2)z\}\sin\{\tilde{a}\sin(\pi\alpha/2)z+\pi\alpha/2\} \\ &-\tilde{a}z\exp\{-\tilde{a}z\} - \frac{(\pi\alpha/2)^2}{6}\exp\{-\tilde{a}z\}(\tilde{a}z)^2(1-\tilde{a}z)\Big\}. \end{aligned} \tag{B22}$$

This may be reduced to

$$g_1(z) \approx \frac{\exp\{-\tilde{a}z\}}{\Gamma(1+\alpha/2)}\left\{1-\frac{(\pi\alpha/2)^2}{6}[1+\tilde{a}z+(\tilde{a}z)^2]\right\}. \tag{B23}$$

Using the facts listed in (B13) and the same procedure as used to approximate $f_2(z)$, we find for $g_2(z)$,

$$g_2(z) \approx \frac{\exp\{-\tilde{a}z\}}{\Gamma(1+\alpha/2)}\left\{\frac{(\pi\alpha/2)^2}{6}[1+\tilde{a}z]+\frac{(\pi\alpha/2)^2}{12}(\tilde{a}z)^2\right\}. \tag{B24}$$

B.3. Matrix shear loads

Substituting the matrix constitutive law (17) and (18) for $s\underline{\mathscr{G}}(s)$ into $T_n^u(\xi, t)$ (23) yields

$$h(\xi, t)/\sqrt{\Gamma(\alpha+1)} = \mathbf{L}^{-1}[s^{\alpha/2-1}\exp(-\hat{a}|\xi|s^{\alpha/2})/\sqrt{\Gamma(\alpha+1)}], \tag{B25}$$

where

$$h(\xi, t) = -\frac{1}{\pi}\int_0^\infty \frac{\exp(-rt)}{r^{1-\alpha/2}}[\exp\{-\hat{a}|\xi|\cos(\pi\alpha/2)r^{\alpha/2}\}]\times\sin\{\hat{a}|\xi|\sin(\pi\alpha/2)r^{\alpha/2}-\pi\alpha/2\}\,dr. \tag{B26}$$

In this case, the integral around the small ε-circle tends to 0 as $\varepsilon \to 0$. Using the same series of variable transformations as above, we get

$$\begin{aligned} h_0(z) &= t^{\alpha/2}h(\xi,(|\xi|/z)^{2/\alpha}) \\ &= -\frac{2}{\pi\alpha}\int_0^\infty [\exp\{-\hat{a}\cos(\pi\alpha/2)zv-v^{2/\alpha}\}] \\ &\quad\times\sin\{\hat{a}\sin(\pi\alpha/2)zv-\pi\alpha/2\}\,dv. \end{aligned} \tag{B27}$$

In this case, we write

$$\exp(-v^{2/\alpha}) = 1-\mathbf{H}(v-\Gamma(1+\alpha/2))-\Delta_z(v), \tag{B28}$$

and break up $h_0(z)$ as

$$h_0(z) = h_1(z)+h_2(z), \tag{B29}$$

where

$$h_1(z) = -\frac{2\Gamma(1+\alpha/2)}{\pi\alpha}\int_0^1 [\exp\{-\tilde{a}\cos(\pi\alpha/2)zv\}]\times\sin\{\tilde{a}\sin(\pi\alpha/2)zv-\pi\alpha/2\}\,dv, \tag{B30}$$

and

$$h_2(z) = \frac{2}{\pi\alpha}\int_0^\infty \Delta_z(v)\exp\{-\hat{a}\cos(\pi\alpha/2)zv\}\sin\{\hat{a}\sin(\pi\alpha/2)zv-\pi\alpha/2\}\,dv. \tag{B31}$$

Applying the trigonometric identity, $\sin(a-b) = \sin(a)\cos(b)-\sin(b)\cos(a)$, we obtain the sum of two integrals for $h_1(v)$ which can be evaluated in closed form to yield,

$$h_1(z) = -\frac{2\Gamma(1+\alpha/2)}{\pi\alpha}\frac{\sin\{\tilde{a}\sin(\pi\alpha/2)z\}}{\tilde{a}z}\exp\{-\tilde{a}\cos(\pi\alpha/2)z\},$$

which is approximately

$$h_1(z) \approx -\exp\{-\tilde{a}z\}\left[1-\frac{(\pi\alpha/2)^2}{6}+\tilde{a}z\frac{(\pi\alpha/2)^2}{2}\right]. \tag{B32}$$

Using the same procedure as used for $f_2(z)$ and $g_2(z)$, we approximate $h_2(z)$

$$h_2(z) \approx -\frac{(\pi\alpha/2)^2}{6}\tilde{a}z\exp\{-\tilde{a}z\}. \tag{B33}$$

As a final step, we add the two components of $f_0(z)$, (B12) and (B14), of $g_0(z)$, (B23) and (B24), and of $h_0(z)$, (B32) and (B33), and for each function, retain the lowest order terms in both z and α. Collecting the coefficients, we obtain the following

$$f_0(z) \approx \exp\{-\tilde{a}z\} + \frac{(\pi\alpha/2)^2}{6}\tilde{a}z\exp\{-\tilde{a}z\}, \tag{B34}$$

$$g_0(z) \approx \frac{1}{\Gamma(1+\alpha/2)}\left[\exp\{-\tilde{a}z\} - \frac{(\pi\alpha/2)^2}{12}(\tilde{a}z)^2\exp\{-\tilde{a}z\}\right], \tag{B35}$$

and

$$h_0(z) \approx -\exp\{-\tilde{a}z\} + \frac{(\pi\alpha/2)^2}{6}[1-4\tilde{a}z]\exp\{-\tilde{a}z\}. \tag{B36}$$

Using the above approximations, $f_0(z)$, $g_0(z)\sqrt{\Gamma(1+\alpha)}$, and $h_0(z)/\sqrt{\Gamma(1+\alpha)}$ are substituted back into $L_n^u(\xi, t)$ (21), $V_n^u(\xi, t)$ (20), and $T_n^u(\xi, t)$ (23), respectively, and the final result presented in Section 3.4 as (50)–(52). Note that as $\alpha \to 0$, $\tilde{a} \to 2\sin(\theta/2)$ and $z = \xi/t^{\alpha/2} \to \xi$, so we recover in (B33)–(B35), the basic exponential term in the linear elastic solutions (43)–(45).

Finally we mention that an error in Laplace inversion in Lagoudas *et al.* (1989) prevents proper recovery of the elastic analytical solution in the $t \to 0$ limit, thus necessitating all new calculations here. This error is not noticeable in numerical plots except at very small times.

APPENDIX C

Here we consider an infinite sequence of fiber breaks on the transverse plane located on the even-numbered fibers $2n$ covering $0, \pm 2, \pm 4, \ldots, \infty$. Suppose these fibers have a break at $\xi = 0$, while the odd-numbered fibers $2n-1$ remain intact. Since all the breaks are aligned and exist on every other fiber, for any two breaks labeled i and j, where $i, j = 1, \ldots, \infty$, $(\xi_i - \xi_j) = 0$ and $(n_i - n_j) = 2n$ for some integer n. Therefore, $\Lambda_{ij}(t) = L_{2n}^u(0, t)$ for some n and has the following form,

$$L_{2n}^u(0, t) = -\frac{1}{2}\int_0^\pi \cos(2n\theta)\sin(\theta/2)\,d\theta, \tag{C1}$$

which applies to the viscous, (31), elastic (43), and viscoelastic (46) or (50) cases. In other words, $L_{2n}^u(0, t)$ is independent of time and α. From (77), (C1) can be expressed simply as,

$$L_{2n}^u(\xi, t)|_{\xi=0} = \frac{1}{4(2n)^2 - 1}, \quad t \geqslant 0, |n| \geqslant 0.$$

The infinite periodicity of the break locations means that each break has the same weighting factor, denoted as K_b. Since all the load transmission functions are time independent from (C1), K_b will be constant. Therefore we can solve for K_b by applying (60) to any one of the breaks.

$$\begin{aligned} -1 &= K_b\left\{-1 + 2\sum_{n=1}^{\infty}\frac{1}{4(2n)^2-1}\right\} \\ &= K_b\left\{-1 + \left(1 - \frac{1}{4}\pi\right)\right\}. \end{aligned} \tag{C2}$$

As a result, $K_b = 4/\pi$. Knowing K_b we can calculate the half break opening displacement $|U_0(0, t)|$ using (57) and (63). Considering the break at $(0, 0)$ we have,

$$U_0(0, t) = K_b V_0^u(0, t) + 2K_b\sum_{n=1}^{\infty} V_{2n}^u(0, t) + \xi = K_b V_0^u(0, t). \tag{C3}$$

In the second line, the summation is identically zero from boundary condition (19c). Evaluation $V_0^u(0, t)$ using (28) or (47) and substituting into (C3), the total break opening displacement is $2U_0(0, t) = 4(t/\pi)^{1/2}$ for $\alpha = 1$ or $2t^{\alpha/2}/\beta$ for $0 < \alpha < 1$. We can also determine the peak bridging stress P_b at $\xi = 0$, which is time-independent. For any bridging fiber, the breaks are located at $2n-1$ distances apart and therefore using (56) and (62),

$$\begin{aligned} P_b &= 2K_b\sum_{n=1}^{\infty}\frac{1}{4(2n-1)^2-1} + 1 \\ &= 2K_b(\pi/8) + 1. \end{aligned}$$

Therefore, $P_b = 2$.